Real Time Navigation Algorithms for LEO Small Satellites using COTS GNSS

Master's thesis project at Hemeria

NATHAN GROISNE

Title

Real Time Navigation Algorithms for LEO Small Satellites using COTS GNSS

Author

Nathan Groisne <groisne@kth.se>

School of Engineering Science, Double degree student in Aerospace Engineering

Abstract

Many satellites in LEO use a GNSS-based navigation system, taking advantage of the GNSS constellations in MEO to enhance navigation capabilities. The thesis work focused on developing the software enabling GNSS-based navigation for Hemeria's future small satellites operating in LEO.

Real time algorithms were developed to perform on board accurate frame conversions based on the International Earth Rotation and Reference Systems Service 2010 convention. The implementation was tested and independently cross-validated using space mechanics libraries and data from *Observatory of Weights and Measures of Paris*. The method was based on the Earth Orientation Parameters, and the balance between autonomy and accuracy was assessed.

In pursuit of an affordable navigation system, a commercial Off-The-Shelf GNSS receiver was used. The navigation solution, derived from single frequency measurements, suffered from a systematic bias caused by the ionosphere. Mitigation strategies with ionospheric corrections were included in the In Orbit Navigator for LEO Satellites (IONOS) simulator. Several attitude control modes were simulated so the effect of spacecraft tumbling versus the availability of GNSS measurements in a degraded situation was quantified.

Through this thesis, algorithms for GNSS-based navigation of Hemeria's small satellites in LEO were developed. The results showed the successful implementation of real time frame conversions at the metre level at best. It was found that the implementation allowed an improved autonomy of the frame conversion at the decimetre level of accuracy over a period of two months.

Titel

Algoritmer för realtidsnavigering av små LEO-satelliter med COTS GNSS

Författare

Nathan Groisne <groisne@kth.se>

Skolan för teknikvetenskap, student med dubbelexamen i flyg-och rymdteknik

Institution

Fastigheter och byggande

Examinator

Huaan Fan, Universitetslektor vid avdelningen för geodesi och satellitpositionering

Handledare

Milan Horemuz, Direktör för avdelningen för geodesi och satellitpositionering

Sammanfattning

Många satelliter i LEO använder GNSS-baserad navigering och drar nytta av GNSS-konstellationerna i MEO för att förbättra navigeringsförmågan. Avhandlingsarbetet fokuserade på att utveckla mjukvaran som möjliggör GNSS-baserad navigering för Hemerias framtida småsatelliter som opererar i LEO.

Realtidsalgoritmer utvecklades för att utföra exakta ramkonverteringar ombord baserat . Implementeringen testades och korsvaliderades oberoende med hjälp av rymdmekanikbibliotek och data från *Observatory of Weights and Measures of Paris*. Metoden baserades på jordorienteringsparametrarna, och balansen mellan autonomi och noggrannhet utvärderades.

I jakten på ett prisvärt navigationssystem användes en kommersiell off-the-shelf GNSS-mottagare. Denna navigeringslösning, som härrörde från mätningar med en enda frekvens, led av en systematisk bias orsakad av jonosfären. I IONOS-simulatorn ingick strategier för att mildra effekterna med jonosfäriska korrigeringar. Flera lägen för attitydkontroll simulerades så att effekten av rymdfarkostens tumlande kontra tillgängligheten av GNSS-mätningar i en försämrad situation kunde kvantifieras.

Genom denna avhandling utvecklades algoritmer för GNSS-baserad navigering av Hemerias små satelliter i LEO. Resultaten visade en framgångsrik implementering av ramkonverteringar i realtid på meternivå som bäst. Det visade sig att implementeringen möjliggjorde en förbättrad autonomi för ramkonverteringen på decimeternivå under en period av två månader.

Acknowledgements

Contents

Acronyms

Chapter 1

Introduction

Satellites became ubiquitous for navigation, climate science and telecommunications. Over the past 50 years, the development of Global Navigation Satellite System (GNSS) constellations in Geostationary Orbits (GEO) enabled precise navigation for ground and air vehicles. The interest in using the GNSS navigation signals in orbit dates back to the Landsat-4 satellite on the 16th July, 1982 with the first spaceborne Global Positioning System (GPS) receiver onboard.

The miniaturisation of GNSS receivers made real time On-board GNSS-based navigation possible. An embedded GNSS system is now a common technique for small satellites navigation, as an alternative to ground tracking systems [51]. Fig. 1.0.2 shows the cumulative number of nanosatellites and CubeSats launches between 1999 and 2023, with a significant increase after 2013. More and more satellites are equipped with a GNSS module.

Figure 1.0.1: Landsat-4 satellite. Credits: NASA
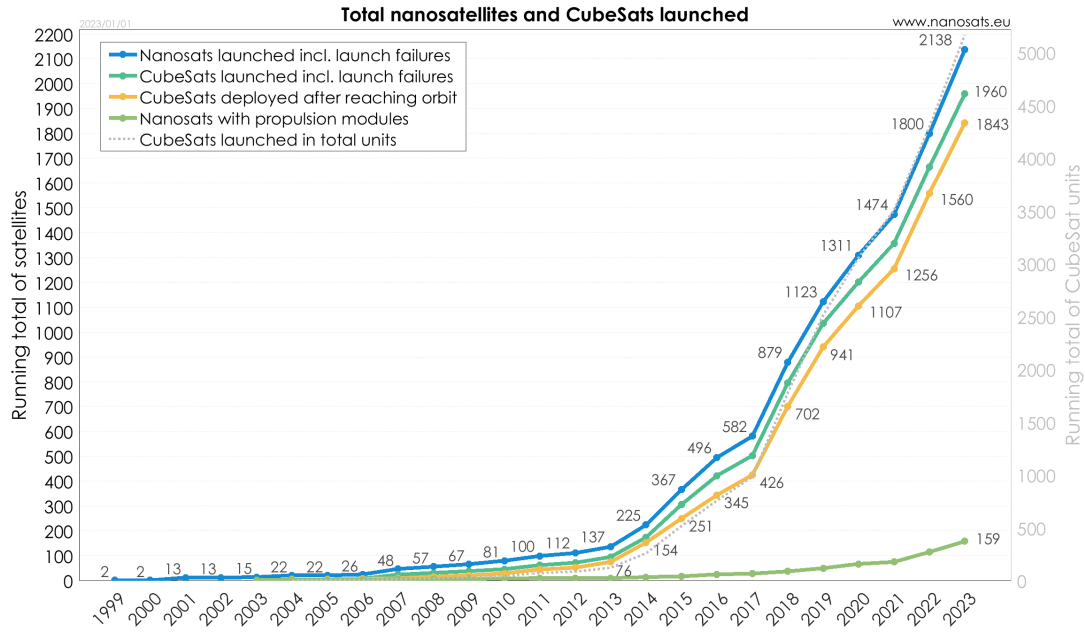
Figure 1.0.2: Nanosatellites and Cubesats cumulative launch number [59]

1.1 Applications of GNSS

GNSS enabled precise positioning, navigation and timing on Earth for numerous applications. Most mobile phones can process GNSS signals. For transportation, GNSS is widely used in automotive navigation systems for positioning and guidance. It is also vital in aviation for navigation and guidance. In maritime applications, GNSS enhances harbour operations for docking and fleet management. Using several antennas, GNSS signals can also be used to derive the orientation of vehicles. GNSS is widely used for land surveying and precise mapping. It is also an active research topic for geodynamics, atmospheric sciences and timing.

Figure 1.1.1: A SiRFstarIII GPS microcontroller Credits: Raimond Spekking

GNSS is used for a wide spectrum of space activities, as reported in [33]. Real-time on-board

navigation is required for formation flying - several satellites performing the same task, sharing the burden - (e.g. GRACE-A and GRACE-B for geodesy from space). Relative navigation for Rendezvous and docking of manned capsules or space cargos also use GNSS (e.g.: Soyouz, Crew Dragon, Automated Transfer Vehicle, ...). Also, the altitude of a space station tends to decrease over it's lifetime due to drag. Thus, it must be estimated to plan thrusts manoeuvres. New applications include GEO satellite servicing, i.e. satellite maintenance on orbit with robotic arms. (e.g. for ESA: ConeXpress - Orbital Life Extension Vehicle (CX-OLEV), Geostationary Service Vehicle (GSV)). For attitude determination (e.g. International Space Station (ISS), satellite platforms), several GNSS antennas can be used. Eventually, precise timing (time-tagging and synchronization of On-Board clock) is also possible.

Another field of application for navigation is Earth Sciences. A very precise Position Velocity and Timing (PVT) information, usually provided by several navigation systems is used to estimate Earth gravitational potential or tidal effects. Also, the navigation signals themselves can be used directly for atmospheric and ionospheric sciences (e.g. Radio Occultation, Scatterometry). Each application exhibits different PVT performance requirements. Earth sciences applications usually have the most demanding requirements. As a consequence, the embedded GNSS receiver and antenna is usually double frequency, heavier and consumes more power. Operations also require a vast spectrum of accuracies. Pointing an antenna to communicate with a satellite or visibility estimation of satellite constellations usually have low requirements.

1.2 LEO missions using GNSS

This section discusses past satellite Low Earth Orbit (LEO) missions using onboard GNSS modules. It emphasises lessons learned from those missions. The interest in Commercial-Off-The-Shelf (COTS) GNSS receivers has developed with the success of radio occultation (RO) experiments [41]. These scientific missions rely on POD (Precise Orbit determination) with GPS receivers On-board. During the past 20 years, a lot of research has been conducted to achieve Precise Orbit Determination (POD) with COTS GNSS receivers [50], [51] and [23], [58]. The COMPASS-1 faced an unexpected behaviour of the onboard GNSS receiver. Due to an improper mechanical integration of the antenna [1], the field of view was limited [12]. Thus, no GPS fixes could be obtained. Latch-up events were experienced by the PROBA-2 spacecraft. As a consequence, the GNSS module was not always activated. The precision achieved was lower than expected. [68] Several student projects have already investigated the topic of navigation with a GNSS receiver. In 2013, Leppinen studied the integration of a

GPS subsystem to the Aalto-1 satellite, with design considerations and a verification procedure [40]. A. Surivet conducted the integration and validation of a nanosatellite flight software [67], using National Marine Electronics Association (NMEA) messages from Argos Neo on a Generic Economical and Light Satellite (ANGELS) satellite. Eventually, the particular case of CubeSats with limited computing and power resources was investigated by S. Weiß [74].

1.3   HEMERIA

The thesis work took place at HEMERIA within the nanosatellite division of the company. The Attitude and Orbit control system (AOCS) work consists in selecting the hardware, create realistic satellite models, design and validate their control laws. Communication with other sub-system teams is also an essential part of the job, providing both quantitative and qualitative inputs related to their expertise in attitude control.

After a 30-year heritage of defence and space expertise, HEMERIA was founded in July 2019 when NEXEYA's historic shareholders decided to strategically refocus the business. NEXEYA thus retained the space and defence businesses, giving HEMERIA the means to focus fully on growing its two highly promising markets. Today, HEMERIA has its headquarters in Toulouse and three other facilities in Angoulême, Ayguesvives and Villebon-sur-Yvette. Together, according to HEMERIA's website [25], these facilities accommodate a total of 400 employees and generates revenue of around 60 M€. In the defence sector, the company participates in the French nuclear deterrent program and on optical tracking systems. In the space sector, HEMERIA does not only work on satellite equipment (wire harness or on-board electronics) but it also produces nanosatellite platforms to host clients' payloads.

HEMERIA designed ANGELS, the first French industrial nanosatellite mission with the help of Centre National d'Etudes Spatiales (CNES) [15]. It was launched in December 2019. ANGELS is a geocompass Earth pointing 12U / 25Kg CubeSat in a 500 km heliosynchronous orbit (see Fig 1.3.1). It embarks the Argos Neo, a miniaturized Argos instrument developed by Thales Alenia Space. Positive results were obtained by both the platform and the payload.

After the previous success, HEMERIA started developing a platform for a 25 nanosatellite IoT constellation for KINEIS. This is still a mission in progress. The satellites will be launched to a polar heliosynchronous orbits at an altitude of 650 km. Each satellite (see Fig. 1.3.2), based on the HP-IOT platform, is a 3-axis controlled platform of almost 16U / 25Kg and is designed to operate for 8 years. At the moment, it is the main project in the company. Furthermore, studies are being carried out in partnership with CNES for a new HEMERIA platform known as HP-EOS which will be used for Earth Observation. This platform will require high pointing and stability.

Figure 1.3.1: Illustration of ANGELS satellite. Credits: CNES/ill. /DUCROS David, 2018

Figure 1.3.2: Illustration of KINEIS satellite. Credits: KINEIS

HEMERIA has a facility at Villebon-sur-Yvette named HEMERIA SERVICES. The facility includes a maintenance laboratory. In 2022, HEMERIA strengthens its activities with the acquisition of Constructions navales et industrielles de la Méditerranée (CNIM) Air Space at Ayguesvives which became HEMERIA AIRSHIP, a European leader in stratospheric, captive and manoeuvring aerostats. HEMERIA created recently the new start-up BLUE WATER INTELLIGENCE of environmental and social utility whose objective is to provide a global and homogeneous decision support system for continental water management.

1.4 Challenges

National Aeronautics and Space Administration (NASA) uses a technology taxonomy to identify, organise technology areas relevant to advancing the agency's mission. NASA identified *Onboard Navigation algorithms* in the field of (AOCS/Guidance Navigation and Control (GNC)) as a technology development discipline needed to enable future space missions [44]. More specifically, a list of challenges was identified during the internship work when it comes to GNSS navigation in LEO:

- When GNSS observables are measured, the PVT information is given in a terrestrial frame [34]. Thus, it is important to implement the Geocentric Celestial Reference System (GCRS)-International Terrestrial Reference System (ITRS) frame conversion on board with a low computational burden. [8] Implementing the International Earth Rotation and Reference Systems Service (IERS) convention on board a satellite relied on external sources providing a set of parameters called Earth Orientation Parameter (EOP). They are determined by several organisations, combining several measurement methods (GNSS, laser ranging, Doppler ranging ...). Nowadays, the message transmitted by the GNSS satellites also broadcasts the EOPs.

- Most of COTS space-grade receivers provide a navigation solution based on uncombined and undifferenced code and/or carrier phase measurement with L1 single frequency only. Most manufacturer do not implement signal combination nor provide access to the raw measurements [42], thus the On-board combination of signals (e.g. GRoup and PHase Ionospheric Correction (GRAPHIC), see GNSS section) is not possible, nor post processing based on pseudorange modelling.

- When the GNSS signal crosses the ionosphere, its path is modified due to the presence of electrons interacting with the signal wave. This is known as the ionospheric delay. Thus, the signal reaches the receiver with some additional delay, introducing an error in the GNSS observations. Experimental models tuned for ground cannot be used at a LEO altitude.

1.5 Purpose

This thesis work aims to enable On-board navigation on commercial small satellites using a COTS GNSS receiver and antenna. Thus, the navigation information given by the GNSS in a terrestrial frame must be converted to an inertial frame for On-Board propagation. The position and velocity precision shall be evaluated. The use of a COTS receiver limits the data at hand and only one frequency for measurements. Mitigation techniques adapted to a LEO spacecraft shall be investigated. Models of physical phenomena shall be gathered to estimate the magnitude of the errors affecting navigation.

The following questions were investigated :

- *How to implement the IERS 2010 convention with improved autonomy ?*

- *Which error sources are dominant in the error budget in the context of a LEO spacecraft ?* [32]

- *Which error sources mitigation methods are suited for real time corrections on board a*

> *LEO spacecraft with a single frequency GNSS receiver providing a navigation solution only ?* [50]

1.6 Methodology

My contribution focused on the development of libraries to implement the IERS 2010 convention On-board autonomously. The convention, defined in [53], was implemented based on a method developed by Bradley [8]. The frame conversion libraries were validated with a space mechanics library and with numerical unit tests from [73]. The gLAB software was used to analyse error sources of the Grace LEO mission in order to understand which effects were predominant, which models were suitable and what data sources were required. [60] A bibliography study was conducted to identify the relevant methods to be used in the context of GNSS real-time navigation in orbit using COTS components. A simulator was developed to compute visibility and dilution of precision of the measurements. It was validated against data from ANGELS' GPS. The orbit of the spacecraft was propagated using an in-house space mechanics propagator on Python. The precise ephemeris of GNSS satellites were extracted from sp3-d files [47].
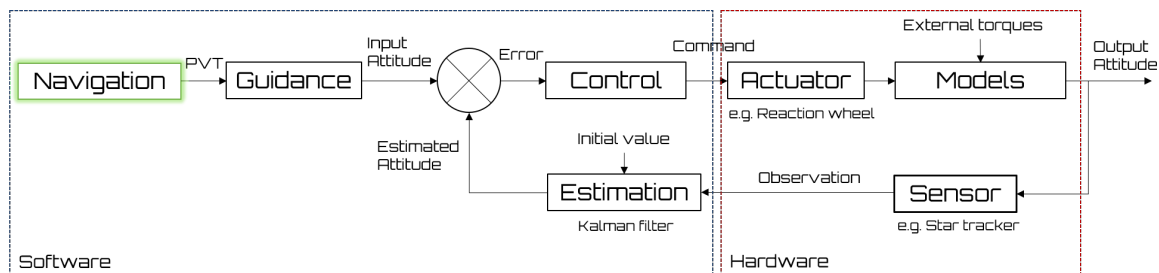
Figure 1.6.1: Attitude control loop from [75]

The thesis work focused on developing the Navigation functional block of the attitude control loop. The PVT information from the navigation system was provided to the attitude guidance algorithm, as described below in Fig. 1.6.1. Based on the PVT information, the target attitude is calculated and given as an input of the attitude control loop.

1.7 Delimitations

The work conducted during the thesis project corresponds to Phase 0 and Phase A of the AOCS/GNC functional chain.[4]

I investigated the use of a GNSS module on a satellite platform providing imperfect navigation information. The work included an important research phase in order to provide a holistic

overview of navigation systems, more specifically about GNSS receivers and mathematical definitions of conventional reference frames. Then, I developed

1. A set of libraries for data analysis to implement the IERS 2010 convention

2. A model of the IERS convention, with a method selected throughout point 1.

3. A simulator, IONOS, to conduct preliminary statistical analysis and to help with antenna mechanical integration.

1.8   Outline

Chapter 2 introduces key concepts of satellite navigation : Satellite orbits, GNSS navigation. Chapter 3 describes the actual work, the difficulties in implementation and how they were solved. Chapter 4 discusses the implementation of IONOS and the simulation results. Eventually Chapter 5 draws a conclusion regarding the features of GNSS navigation.

Chapter 2

Satellite navigation

Satellite navigation is part of spacecraft operations. Knowledge of the current position, velocity and clock time of the spacecraft is essential for planning manoeuvres, determining, predicting and correcting the orbit of a satellite [23].

2.1   The Global Navigation Satellite System
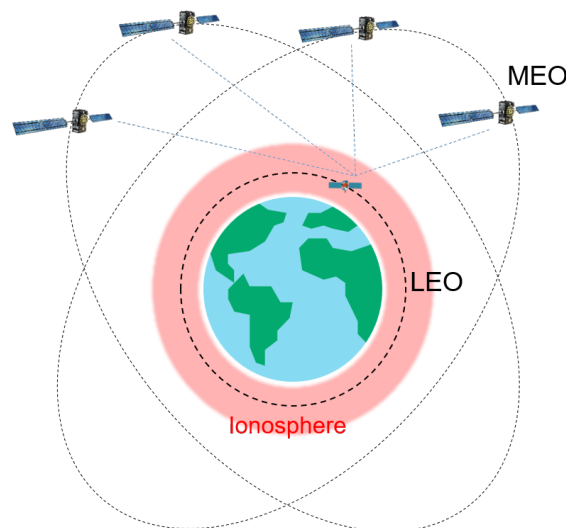
Figure 2.1.1: LEO satellite and four Galileo satellites

The GPS was developed in the 1970s by the United States. The first satellite was launched in 1978. Each satellite transmits a Pseudo Random Noise (PRN) and a navigation message. The PRN is used by receiver to estimate a *pseudorange*. The delay between the time of transmission and reception by the receiver is obtained by comparing the received PRN with the PRN code in the receiver. Three satellites are required to estimate position and a fourth is required to solve for the receiver clock bias. LEO satellite with receiver has unknown coordinates (x_r, y_r, z_r) and

a GNSS satellites has known coordinates (x^s, y^s, z^s). GNSS observables are the pseudoranges P_0^i.

$$
\begin{aligned}
\rho_0^1 &= \sqrt{(x^1 - x_r)^2 + (y^1 - y_r)^2 + (z^1 - z_r)^2} \\
\rho_0^2 &= \sqrt{(x^2 - x_r)^2 + (y^2 - y_r)^2 + (z^2 - z_r)^2} \\
\rho_0^3 &= \sqrt{(x^3 - x_r)^2 + (y^3 - y_r)^2 + (z^3 - z_r)^2} \\
\rho_0^4 &= \sqrt{(x^4 - x_r)^2 + (y^4 - y_r)^2 + (z^4 - z_r)^2} \\
P_0^i &= \rho_0^i + c \cdot \delta_r^s
\end{aligned}
\tag{2.1}
$$

There are four constellations with global coverage : GPS, Galileo, GLONASS and Beidou (former Compass). There are two other regional systems, Quasi-Zenith Satellite System (QZSS) and Indian Regional Navigation Satellite System (IRNSS). Fig. 2.1.2 shows the trajectories of GPS and Galileo satellites obtained from a precise ephemeris file, over one day.
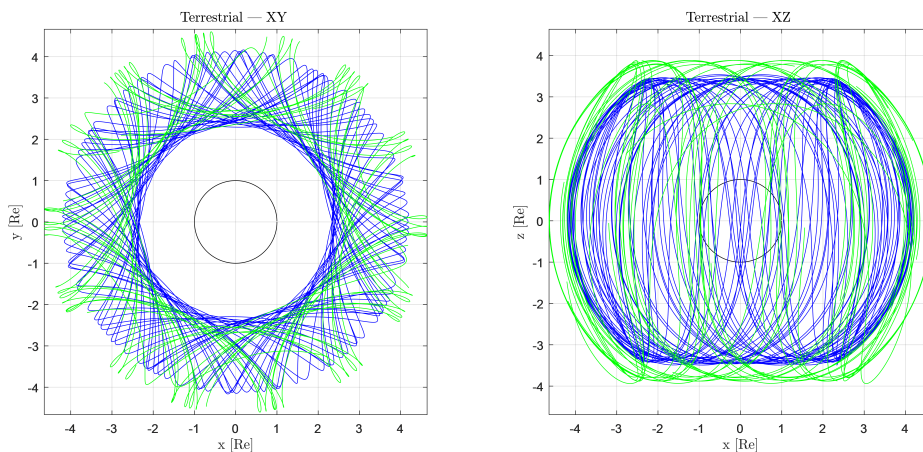
Figure 2.1.2: GPS (blue) and Galileo (green) constellations, ECEF frame

Table 2.1.1: GPS and Galileo constellations average ephemeris

Characteristic	GPS	Galileo
Number of satellites	24-36	24-30
Orbit altitude (km)	20 200	23 222
Eccentricity	4×10^{-4} - 2×10^{-2} [35]	1×10^{-4} - 5×10^{-4} [36]
Orbital period	11h58m2s	14h4m41s
Number of planes	6	3
Inclination (deg)	55	56
Speed in ECI (km/s)	3.9	3.7

2.1.1 Error budget

Errors affecting the GNSS observations can be grouped into three quantities: User Range equivalent error (UERE), User Equipment Error (UEE) and Signal In Space Ranging Error

(SISRE). The errors were assumed to have a zero mean. The error associated to each measurement were supposed to be uncorrelated. UERE is calculated by taking the root sum squared (RSS) of SISRE and UEE :

$$UERE = \sqrt{SISRE^2 + UEE^2} \tag{2.2}$$

UERE quantifies the error along a receiver-satellite vector. All UEREs were supposed to have the same variance. [5] SISRE is the Signal in Space Ranging Error. It accounts for :

- Clock errors δt^s: due to noise, interference, multipath in the control segment receivers, aging, temperature sensitivity of the clocks on GPS satellites, and modelling error of the clock bias. Typically 0.3 m. It can be corrected with the broadcasted navigation message (the GPS Interface Control Document (ICD) details the procedure), correcting the relative effects of orbit eccentricity, Satellite group delay (a lag between the time at the satellite clock and the signal leaving the antenna, due to the propagation of the signal in the cables. It is temperature and frequency dependent, typically 0.1 m)

- Ephemeris error $\delta\rho$: the estimation and prediction process of GNSS ephemerides. Typically 0.3 m.

Considering the standard deviations of each source, where E denotes the expected value :

$$
\begin{aligned}
\sigma_{\text{ts}} &= \left(\text{E} \left[(\delta t^s - \text{E}(\delta t^s))^2 \right] \right)^{1/2} \\
\sigma_{\rho} &= \left(\text{E} \left[(\delta\rho - \text{E}(\delta\rho))^2 \right] \right)^{1/2}
\end{aligned}
\tag{2.3}
$$

$$SISRE = \sqrt{\sigma_{\text{ts}}^2 + \sigma_{\rho}^2} \tag{2.4}$$

Using sp3 data as the source of GNSS data for IONOS allows to retrieve the uncertainty of ephemeris for each satellite (in the header section of the sp3 file). Also, GNSS clock offsets and hardware delay are accounted in the sp3 file, so no additional correction is required.

UEE is the User Equipment Error. It accounts for

- Atmospheric delay. Only ionospheric delay was accounted. The zero mean error is particularly wrong for the ionospheric delay.

- Receiver Group Delay error

- Multipath : Due to the clear sky visibility conditions, *multipath was neglected.*

- Noise and interference *were neglected.*

$$\begin{aligned} \text{UEE} \quad &= \quad \sqrt{\sigma_{\delta I_{L1}}^2 + \sigma_m^2 + \sigma_\nu^2} \\ &\simeq \quad |\sigma_{\delta I_{L1}}| \end{aligned}$$

(2.5)

Table 2.1.2: UEE error sources budget for a LEO spacecraft

External Model correction	Model for mitigation	Model bias [m]	σ
Ionospheric delay	NeQuick-G or NTCM-G, position-dependent, space weather dependent	10 (low solar) - 100 (high solar)	5-10 TECU
Multipath (Rx)	Stochastic model [21] or Sigma multipath (Elevation or SNR dependant) or constant [60]	0 m	1-100 m

Enventually, UEE only accounts for the ionospheric delay in the assumptions.

Dilution Of Precision (DOP) is a parameter which relates the standard deviations of measurement errors to the standard deviation in position:

$$\sigma_{\mathbf{x}} = \sqrt{\sigma_x^2 + \sigma_y^2 + \sigma_z^2} = \text{PDOP} \cdot \text{UERE}$$

(2.6)

DOP is dependent on the user-satellite geometry [39]. It is independent of the precision of the measurement. UERE reflects the precision of the measurements. DOP is computed using the geometry matrix $\mathbf{G}$ (e.g with four satellites in view) :

$$[\mathbf{G}] = \begin{pmatrix} \widehat{\boldsymbol{\rho}}_0^1 & 1 \\ \widehat{\boldsymbol{\rho}}_0^2 & 1 \\ \widehat{\boldsymbol{\rho}}_0^3 & 1 \\ \widehat{\boldsymbol{\rho}}_0^4 & 1 \end{pmatrix}$$

(2.7)

where each line of the geometry matrix is a unit vector corresponding to the line of sight from receiver 0 to GNSS satellite j :

$$\widehat{\boldsymbol{\rho}}_0^j = - \left(x_0 - x^j, y_0 - y^j, z_0 - z^j \right) / \left\| \left(x_0 - x^j, y_0 - y^j, z_0 - z^j \right) \right\|$$

(2.8)

When five satellites or more are used in the positioning process, the problem is over constrained. Thus a least square estimation of the position and receiver clock bias is performed.

The unknowns ($\delta \mathbf{x}$ and δ t) are represented by [$\delta \hat{\mathbf{y}}$] and they are related to range error $\delta \rho$. Assuming all measurements have the same, the least square solution is given by [22]:

$$[\delta \hat{\mathbf{y}}] = \left([\mathbf{G}]^T [\mathbf{G}]\right)^{-1} [\mathbf{G}]^T \delta \rho \qquad (2.9)$$

and the covariance matrix of the estimated ranges is given by [22]:

$$E\left([\delta \hat{\mathbf{y}} \delta \hat{\mathbf{y}}^T]\right) = \sigma^2 \left([\mathbf{G}]^T [\mathbf{G}]\right)^{-1} \qquad (2.10)$$

Defining matrix $[\mathbf{H}] = ([\mathbf{G}]^T [\mathbf{G}])^{-1}$, DOPs were computed as :

$$
\begin{aligned}
\text{GDOP} &= \sqrt{\text{Tr}(\mathbf{H})} \\
\text{PDOP} &= \sqrt{\text{Tr}(\mathbf{H}_{3\times 3})} \\
\text{TDOP} &= \sqrt{\text{Tr}(\mathbf{H}_{4,4})}
\end{aligned}
\qquad (2.11)
$$
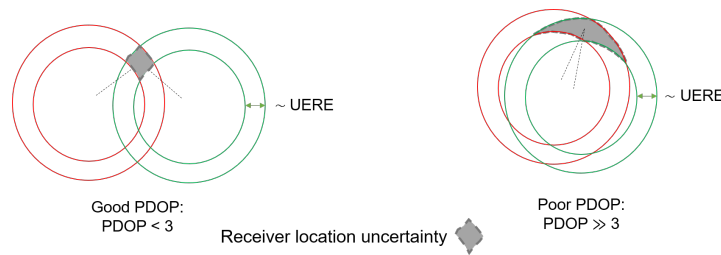
Figure 2.1.3: DOP and satellite geometry

The more satellites in view, the more precise the position estimation.

Clocks On-board GNSS satellites are shifted by a small amount of the nominal frequency of the navigation message. This shift accounts for the special and general relativity.The relative velocity of GPS satellites compared to ground-based atomic clocks means that GPS clocks lag behind ground-based clocks by 7 μs per day. Inversely, the lower gravitational potential experienced by the GPS satellites result in a positive drift of 45 μs per day. The total effect amounts to +37 μs. Ashby derived the frequency shift [3] which is -4.57 mHz, i.e. $f = 10.22999999543$ MHz. As a result, GPS clocks were set to this frequency before they were launched.

In a LEO orbit, the special relativity, i.e. time dilation, dominates the relativity effects due to the high velocity of the receiver. The typical velocity of a LEO spacecraft is 7-8 km/s, while the velocity of a ground-fixed receiver is about $\simeq 0.4$ km/s in a Earth-Centered Inertial (ECI) frame. A GPS receiver oscillator is configured to pulse at a 10.23 MHz, thus it will experience a time lag due to its high velocity. This will have two effects : the observed receiver time will

drift from the GPS time. The second effect is the Doppler shift of the carrier frequency (at 1575.42 MHz for L1 frequency). Thus a larger Doppler window than ground receivers will be required. Also, gravitational frequency shift and Doppler shift are not constant due to the orbit eccentricity.

The validity of this correction was questioned for highly eccentric orbit. With the work of [3], the correction was found to be consistent with the theory within 2%. Results from TOPEX satellite have shown that this correction can be used for LEO spacecraft. A perfectly circular orbit is characterised by $e = 0$ so the eccentric correction is also zero. Eccentric corrections for GPS orbit are typically less than 0.02 [35]. This correction is usually performed by the user. During the signal flight time, the Earth rotates so does any Earth-Centered, Earth Fixed (ECEF) frame (e.g. International Terrestrial Reference Frame (ITRF)). Given a signal flight time of approximately 70 ms from GPS to LEO, it amounts to 30 m offset [28]. This is known as the Sagnac effect. It should be noted that there are second-order effects of special relativity, such as the Shapiro effect (which affects the signal delay, about 2 cm) the geodetic distance shifts due to spatial curvature and other solar system bodies. These effects were not discussed because their magnitude is too small compared to the other sources of errors. The breakdown of relativistic effects are listed in the next table :

Table 2.1.3: Relativity errors accounted in GNSS navigation message

Clock correction	Correction	Error source [m]
Orbit eccentricity [**R**]	Δt_r from Navigation message	0 - 13
Time dilation, Gravitation	- 7 μs/day + 45 μs/day (GPS)	$\sim 11\,000$
Relativistic path range effect [60]	Neglected	0.04
Sagnac effect [**R**]	Corrected by user with Earth rotation rate	30

There are other parameters to consider for GNSS navigation. These parameters are not directly used in a Single Point Positioning process, but they may introduce additional bias.

Table 2.1.4: Other error sources

Effect	Correction method	Bias	Uncertainty
Inter-constellation time offset (GGTO)	Neglected	5-15 [ns] [7]	0 or filtering
ECI/ECEF conversion	EOPs analysis	0.25 m/day	past data: 30 µas (x_p, y_p), µs (UT1-UTC)
GNSS frame realisation offset to ITRF2014 [34]	Neglected	0.01 m (GAL) - 0.16 m (BEI)	Neglected

Examples of scenarios affecting the UERE and $\sigma_{\mathbf{x}}$ were discussed. This section is meant to emphasize the conservative hypothesis of the performance indicated in receivers datasheet. It should be used as a scaling factor of the predicted performance. It was made as accurate as possible relying on state-of the art models of ionospheric delay Neustrelitz Total Electron Content Model (NTCM)-G. The following properties were identified as desired before implementing and validating a model into a simulator presented in IONOS Section.

1. Dominant in the error budget

2. Model with strong research background and suitable to LEO

3. Not already corrected in the positioning process

Eventually, we consider only the following error sources :

$$\text{UERE} = \sqrt{\sigma_{\mathrm{t}^s}^2 + \sigma_{\rho}^2 + \sigma_{\delta I_{L1}}^2} \tag{2.12}$$

A simpler model was proposed by in [29]:

$$\text{UERE} = a + b \exp(-\text{elev}/c) \tag{2.13}$$

where parameters a, b, c would be tuned with real measurement data. This model yields an elevation dependent UERE. The ionospheric error and the multipath error tend to increase when elevation is low. Also, the constant term a accounts for near-constant error (ephemeris error, receiver noise). The error budget of a GNSS-based navigation solution was discussed in the context of a LEO satellite. Relativistic effects, clock errors and ionospheric delay have been examined to understand how they affect GNSS measurements. Range measurement error and

positioning error were also discussed.

2.1.2   Data sources

Receiver Independant EXchange Format (RINEX) 4.0 navigation and observations files from real missions (GRACE, JASON) in LEO are available from [26]. This is the latest version of RINEX (on February 2023). Specific changes include the ionospheric coefficients which are used in the ionospheric model NTCM-G.

Precise ephemeris from the final products sp3-d files were downloaded from [47]. ESA0MGNFIN_20182750000_01D_05M_ORB.sp3 was used to run the simulations. Final, Rapid and Ultra-rapid products denote data files (with ephemeris, clock and EOP). Each product have different sampling rates and release delays. The data used in this work was the final product. It had a sampling rate of five minutes, over a period of one day. It contains the ECEF coordinates of the GPS, Galileo, GLONASS, BEIDOU and QZSS satellites. The header contains the starting epoch, the number of satellites observed, the PRN which identifies each satellite in a constellation. There is also the precision of the estimated position.

(a) sp3 header

(b) Example of precise ephemeris data

Figure 2.1.4: Precise ephemeris - Final product

NMEA is a protocol used by GNSS receivers to provide a PVT information. NMEA-0183 is the current protocol. The information is disseminated in different *messages*. A receiver does not necessarily provide all the message. For example, the message GSA provides GPS DOP and active satellites, and message GST provides Position error statistics [69]. An example of GSA message is provided below :

$GPGGA,172814.0,3723.46587704,N,12202.26957864,W,2,6,1.2,18.893,M,-25.669,M,2.0,0031*4F

The position was estimated at 20:21:34.00 Coordinated Universal Time (UTC). Latitude is 37°23.465" in the North direction, Longitude is 12°202.26957864" in West direction. The next field refers to the quality indicator, 2 is for measurement performed by a receiver with respect to a ground station (pseudorange differential). There were 6 satellites used (different from the number in view). Horizontal Dilution of Precision (HDOP) is 1.2. Antenna was at altitude 18.893 m above the sea level. M indicates meters. The next field indicates undulation (relation between geoid and WGS84 ellipsoid). The penultimate field is the age of correction data in seconds, and the last field in the ID of the ground station.

2.1.3 GNSS receivers

Table 2.1.5 lists GNSS receivers, from oldest to newest. The number of tracking channels, the standalone maximum power consumption of the receiver (i.e. without any active antenna connected), the standalone mass of the receiver, User range accuracy (URA), Total Ionization Dose (TID), Time To First Fix (TTFF) and frequency bands acquired by the receiver were indicated. The last year of launch was indicated, with flight heritage when available. Several data sheets of receivers were analysed. Different metrics in the data sheets were used (CEP, Horizontal 2D Root Mean Square (RMS), Radial RMS, 1 σ, 3 σ). Consistency of the reported URA with the different error definitions was taken into account, according to [16]. The values indicated should be considered as typical values in optimal scenario. A detailed error sources budget was given in the dedicated section. Table 2.1.5 shows that dual frequency receivers have a higher mass than most single frequency receivers. The lowest power consumption is Warpspace with 100 mW. The lowest mass is u-blox with 1g. The URA ranges from 1.5 to 10 meters. TID information was not often available. TID was found to range from 5 to 30 krads. This parameter is particularly important to estimate the availability of a GNSS receiver. Only TopStar, OEM and Phoenix provide raw code and phase measurements. The other receivers provide a navigation solution with the NMEA protocol, described below. Access to raw measurements allows phase and code measurements to be combined. In this way, certain biases can be removed from the observations.

2.2 Models

Methods for kinematic and dynamic positioning of a LEO spacecraft were detailed in [60]. Post processing techniques of various sources of data (including GNSS observations) are often used to determine precisely the orbit of a spacecraft. Kalman filtering, point mass filtering and Lagrangian interpolation are common techniques in spacecraft navigation.

Table 2.1.5: Space grade GNSS receivers for LEO satellites, sorted from old to new. Rx = Receiver, Ch. = Number of tracking channels, URA = User Range Accuracy, Single Point Positioning L1 in LEO. Navigation solution accuracy. Measurement accuracy is *not* indicated. TID = Total Ionizing Dose. TTFF = Time to first Fix, Cold & Warm start. Year = latest launch year. Mass = receiver mass. Receivers with * symbol are COCOM limited. Note even COCOM-free receivers may not work in GEO or HEO. +S in Bands = SBAS handling capabilities [41] [45] [74] [2] [66]

Manuf.	Rx.	Ch.	P [W]	m [g]	URA [m]	TID [krad]	TTFF	Bands	Year	Legacy
Alcatel [31], France	TopStar 3000	30 C/A	10	1500	L1	> 30		TBD.	2001	Demeter, Kompsat 2
Novatel, Canada [48]	OEM4-G2L*	24	1.6	56	1.8	Unk.	50/40 s	L1,L2, +S	2009	CanX-2, AISSat-1
DLR, Germany [17]	Phoenix	12 C/A	0.85	22	10	> 10	10/3 min	L1	2009	Compass-1, UWE-2, PROBA-2, X-Sat, FLP, ARGO, PRISMA
Novatel, Canada [49]	OEMV-1*	36	1.0	21.5	1.5	Unk.	60/35 s	L1, +S	2011	RAX-1, RAX-2
SSTL, UK [61]	SGR-Axio	24 C/A	4	1000	5	≥ 5	120	L1, L2C	2018	Unk., 4 satellites
NavSpark	Venus, 838FLPx	167 C/A	0.11	0.3	2.5	Unk.	29/1 s	L1	2018	Unk.
SSTL, UK [62]	SGR-Ligo	24 C/A	0.5	90	5	5	90	L1	2019	Unk., 2 Cubesats
General Dynamics, USA	Viceroy-4	12	8	1.1	15	Unk.	4/Unk. min	L1	2019	Unk., 20 yrs. in orbit legacy
GomSpace [24], Denmark	GPS-kit	TBD	1.3	31	1.5	Unk.	Unk.	Unk.	2019	Unk, TRL 9
ublox [70]	NEO-M8*	72	0.18	1	2.5	TBD	29/1 s	L1, +S	2019	Astrocast
SkyFox Labs [65]*, Czech Republic	piPATCH, L1E1	TBD	0.07	50	Unk.	Unk.	Unk.	L1	2020	Unk., TRL 9
AAC Clyde Space, Sweden	GNSS-701	55	0.9	188	1.5	10	40/19 s	L1	2022	AprizeSats, Genesis, FASTSat ...
SpaceManic, Slovakia	Celeste	Unk.	0.1	25	2	Unk.	29/1 s	Unk	2022	Unk.
Warpspace, Japan	Warp space	167 C/A	0.15	3	2.5	TBD	29/28 s	L1, +S	Unk.	TRL 6

2.2.1 Perturbations model

A model of the forces acting on the spacecraft is required to derive the accelerations and propagate the position and velocities over the orbit. The models used in the implementation are described. The two body problem is an simplification of reality. The additional accelerations must be accounted as small disturbances to the idealised situation.

Table 2.2.1: Acceleration breakdown at 780 km altitude, [43]

Phenomenon	Amplitude (km/s²)	Included
Two body attraction	1×10^{-2}	✓
J_2 zonal harmonic	1×10^{-5}	✓
$J_{2,2}$ tesseral harmonic	1×10^{-7}	✓
$J_{6,6}$ tesseral harmonic	1×10^{-8}	✓
Moon and Sun	1×10^{-9}	✓
Atmospheric drag	$1 \times 10^{-12} \rightarrow 1 \times 10^{-9}$	✓
$J_{18,18}$, Dynamic solid tides	$< 1 \times 10^{-9}$	✓ / No
Solar radiation pressure	1×10^{-10}	✓
Relativistic effects on acceleration	1×10^{-11}	No
Venus and Jupiter gravitation pull	1×10^{-14}	No

1. Non-spherical Earth : While Earth's shape is well approximated by an ellipsoid (WGS84 was used), it's density and geometry is not uniform. Thus a latitude and longitude dependent potential gravitational potential was proposed by [27]

$$
V = \frac{\mu}{r} \left[1 - \sum_{n=2}^{\infty} \left(\frac{a_E}{r} \right)^n J_n P_n(\sin \phi) \\
+ \sum_{n=2}^{\infty} \sum_{m=1}^{n} \left(\frac{a_E}{r} \right)^n \left(C_{nm} \cos m\lambda + S_{nm} \sin m\lambda \right) P_{nm}(\sin \phi) \right]
$$

(2.14)

a_E is Earth equatorial radius, μ is the Earth gravitation parameter, r is radial distance to geocenter, λ is the geocentric longitude and ϕ the geocentric latitude. C_{nm} and S_{nm} denote the zonal (m = 0) and tesseral coefficients of the harmonic development known from a model of Earth. 30 zonal terms and 30 tesseral terms (30 × 30) gravity model were used for the orbit propagation.

2. The Moon and the Sun produce perturbing forces acting on the satellites. They also induce tidal effects on Earth, but the effect is negligible.

3. The solar radiation pressure : the photons impact the spacecraft, causing additional

acceleration. It is dependent on the reflective properties and area to mass properties of the spacecraft.

4. Atmospheric drag : NRLMSISE00 was used to model the atmospheric density and temperature. The solar wind directly affects the atmosphere composition and shape so it must be modelled. A Marshall solar activity model was used.

5. Several other effects could be included in the model. The perturbation accelerations at 780km altitude are break-downed in Table 2.2.1 according to [43].

There are several models for orbit propagation in an inertial frame (Keplerian, Secular J2, Eckstein-Heckler, Lyddane-Brouwer, SGP4) [10]. A in-house propagator was used, allowing to tune each individual model. Propagation in the ITRF frame is also possible. It requires two additional accelerations, the Corriolis effect and the centrifugal force. This method is fundamentally different because it does not require to transform coordinates from ITRF to GCRF. However, the propagator needs to compute the satellite's orbit in the ITRF. The knowledge of additional accelerations requires an approximate knowledge of TAI-UT1 as well. This method was not investigated further.

2.2.2 Pseudorange and Phase equations

The pseudorange equation relates the measured range P to the geometric distance ρ , riddled with biases and noise. [6] (2.15) models the bias affecting the pseudorange.

$$P_1 = \rho + d\rho + c\left(\delta t_r - \delta t^s\right) + I_{\mathrm{L}1} + m + \nu \tag{2.15}$$

The dominant term is ρ, the true range between receiver and satellite, $\simeq 20000$ km. The ephemeris error $d\rho$ ranges from ~ 0.2 m for Galileo to ~ 3 m for Beidou. δt_r is the receiver clock error and δt^s is the satellite clock error. The receiver clock error is unknown. It drifts in time and typical clock steering strategies reset the clock with an offset of 0.1 μs from the GPS time scale.

$$L_1 = \rho + d\rho + c\left(\delta t_r - \delta t^s\right) - I_{\mathrm{L}1} + m + \nu + \lambda N \tag{2.16}$$

Ranges can also be estimated by measuring the phase of the carrier signal. The total number of cycles is unknown, it is called integer ambiguity (λ N). The phase measurement is more precise than the range measurement but it is ambiguous. The carrier phase equation models the phase and accounts for error sources in the measure.

Unlike scientific satellites with dual frequency GNSS receivers onboard which can reach a 10

cm real time accuracy in LEO, the Position, Velocity and Timing requirements for Attitude Control Systems of a small satellite are far less. Past missions using state-of-the art receivers for spacecrafts were investigated, suggesting a real time accuracy in LEO of 1.5 m.

The GRAPHIC combination is defined as

$$G = \frac{P_1 + L_1}{2} \tag{2.17}$$

where P_1 is the Coarse Acquisition (C/A) code ranging signal and L_1 is the phase signal at L_1 frequency. The GRAPHIC combination is widely used for satellite navigation because it needs only one frequency (e.g. L1) to remove the first order ionospheric effect. Moreover, the ambiguity is an integer for GRAPHIC.

The following table shows the biases corrected by each combination. A cell with ✓ means that the first order bias is cancelled by the combination. The second order effect of the ionospheric delay contributes up to a few centimeters. The Ionofree combination also removes the ionospheric effect but requires two frequencies and has a non integer ambiguity. GRAPHIC is particularly interesting as it requires only a single frequency receiver, which is the case for most COTS GNSS receivers.

Table 2.2.2: Uncombined and combined GNSS measurements. σ_1 is the standard deviation of the code measurement

Combination	Symbol	Clock delay	Ionospheric delay	Ambiguity	σ/σ_1
C/A Code	C1	X	X	0	1
Carrier Phase	L1	X	X	Integer	~ 0.01
GRAPHIC	G	✓	✓	Integer	$= 1/2$
Ionofree	L$_I$	✓	✓	Float	$\simeq 2.02$
Single-difference	∇P	✓	X	Integer	$\simeq 1.41$
Double-difference	$\Delta\nabla P$	✓	✓	Integer	2
Triple-difference	$\nabla\Delta\nabla P$	✓	✓	0	2.82

2.2.3 Atmospheric effects

LEO orbits altitudes range from $\sim$ 250 km to 2000 km. These altitudes are above the troposphere which extends up to 15 km. Thus the tropospheric effect can be removed from the analysis. The ionospheric effect is less important than on ground because the signal path through the ionosphere is shorter. Yet, it has a significant impact on the error budget for LEO orbits between 250 and $\simeq$ 1200 km. The integrated electron density along the signal path determines the ionospheric delay. The density can be modelled by a Chapman profile, and its maximum varies between 200 and 400 km, depending on the time of day and solar activity. The residual electron content above the LEO altitude may impact the navigation solution. The actual value of the ionospheric delay is highly dependent on the solar activity [18] and the user location. The ionospheric delay, expressed in meters, is defined as :

$$I_\phi = -I_\rho = \frac{40.3\text{TEC}}{f^2} \tag{2.18}$$

The Klobuchar models assumes the whole electron density profile is confined to a thin layer profile, roughly at 350 km altitude (which is the maximum density of the electron profile [18]). The coefficients of the Klobuchar model are broadcasted in the navigation message of GPS. Inputs are :

- The local time t

- Elevation of GPS satellite and latitude of ground station

- Broadcasted coefficients α_i, β_i with i = 0,1,2,3

When the GNSS signal crosses this thin layer, the signal is delayed. The model provides the Vertical Total Electron Content (VTEC) quantity, it describes the delay of a signal vertical to the station. VTEC is mapped onto Total electron content along the signal flight path (STEC) with the elevation to obtain the delay along the station-satellite vector. This model is tuned for ground user, thus one cannot use this model in LEO unless some scaling strategy of the Klobuchar coefficients is used. This strategy relies on global maps of Total Electron Content (TEC) to find the scale factor. New models do not rely on the thin layer assumption and allow a 3D estimation of the STEC.

NeQuick-G and NTCM-G models are more suited to model the ionospheric activity for a LEO spacecraft. They do not rely on a thin layer approximation, so the TEC can be used for all altitude. According to the Galileo ICD, the effective ionisation coefficients quantify the intensity of the ionospheric activity due to the solar wind (a_{i0} is given in solar flux unit). NTCM-G is a simplified version of NeQuick-G, more suitable for On-board implementation. The NTCM-G

documentation indicates typical values for low, medium and high activity :

$$
\begin{aligned}
(a_0, a_1, a_2) &= \quad (2.580271 \quad \text{sfu}, 0.127628236 \quad \text{sfu/deg}, 0.0252748384 \quad \text{sfu/deg}^2) \\
(a_0, a_1, a_2) &= (121.129893 \quad \text{sfu}, 0.351254133 \quad \text{sfu/deg}, 0.0134635348 \quad \text{sfu/deg}^2) \\
(a_0, a_1, a_2) &= (236.831641 \quad \text{sfu}, -0.39362878 \quad \text{sfu/deg}, 0.00402826613 \quad \text{sfu/deg}^2)
\end{aligned}
\tag{2.19}
$$

(units are Solar Flux Unit (sfu), sfu/deg and sfu/deg²). Provided that a ionospheric activity state is available, the values of the coefficients could be set to the precedent values. Otherwise, the set (63.7, 0.0, 0.0) corresponds to the minimum solar activity so it should be used when no other option is available. [14].

Table 2.2.3: NTCM inputs

Parameter NTCM	Description	Source for off-line analysis	Source - OnBoard real time
a_{i0}, a_{i1}, a_{i2}	Effective ionisation coefficients	RINEX 4.00 nav. file, Option 2 : Set default value	Option 1 : Galileo Navigation message Option 2 : Set default value
$\varphi_u, \lambda_u, h_u$	User geodetic* latitude, longitude and height	Conversion from GCRF	NMEA message
$\varphi_s, \lambda_s, h_s$	Satellite geodetic* latitude, longitude and height	Conversion from GCRF	NMEA message
UT	Universal time	Converted from TAI	Converted from OnBoard Time (OBT)

The NTCM model provides the STEC value for each satellite receiver vector. The navigation error due to the ionospheric delay is [42]:

$$
\Delta \text{iono} = (\mathbf{G}^{\mathrm{T}}\mathbf{G})^{-1}\mathbf{G}^{\mathrm{T}}\mathbf{I}
\tag{2.20}
$$

$$
\mathbf{I} = \frac{40.3}{f_{\mathrm{L1}}^2}\mathbf{STEC}
\tag{2.21}
$$

G is provided by a preliminary analysis of the GNSS constellation. **STEC** is provided by the NTCM model.

2.3 Other navigation systems

The tracking systems available on ground were discussed in the following section in terms of observed accuracy, autonomy, availability and robustness. Advantages and drawbacks were compared for each tracking system.

2.3.1 DORIS

The Doppler Orbitography and Radiopositioning Integrated by Satellite (DORIS) system is described in the following paragraph. It is an uplink radio system based on the Doppler principle. The user satellite relies on a global network of ground-based tracking stations that provide accurate measurements for POD. The concept is to reverse the GNSS principle: satellites are equipped with DORIS receivers and measure the Doppler shift of the signal emitted by ground stations. There are more than 50 stations uniformly distributed on ground. [43] (p. 202) DORIS receivers are dual frequency beacons at 401.25 MHz and 2.036 GHz.

DORIS is a French navigation system designed and optimized by the CNES, the IGN *Institut Géographique National*), and the GRGS (*Groupe de Recherches en Géodésie Spatiale*) for high precision orbit determination, reference frame determination and scientific study of the ionosphere [19]. Analysis of the SPOT-5 mission shows a real time 3D RMS accuracy of 5 m in position, 2.5 mm/s for velocity and 3 μs for timing. [57] According to the CNES technology reference [11], precision is ≤ 1 m , velocity precision is 0.3 mm/s, and timing precision is ≤ 5 μs RMS. The first satellite with DORIS onboard was SPOT2 in 1990. TOPEX, JASON, ENVISAT, CRYOSAT, HY, SENTINEL and SWOT were also equipped with DORIS beacons mainly for altimetry [19].

Figure 2.3.1: DORIS tracking station

Autonomy : 15 uploads/year (Version 1), On board update (Version 2)

Availability : 363 days over 365 i.e. 99.5 %

Robustness : Error inferior to 50 m during semi-major axis raising manoeuvre of 8 km.

2.3.2 SLR

Satellite Laser Ranging (SLR) is commonly used to obtain accurate orbit determination. External validation of other orbit determination techniques can be performed with SLR. The RMS accuracy is of the order of 1 cm. Pulses of green laser light at 532 nm are emitted at a frequency of 5-10 Hz for 30 to 200 ps. Time accuracy is better than 1 µs when the receiver clock is regularly updated with GPS time. Antenna pointing requires an a priori very accurate orbit. It is subject to meteorological variations and the availability of observatories is very low.

Figure 2.3.2: Laser Ranging Station in Tenerife [56]

Table 2.3.1: Trade-off analysis - Real time onboard navigation performance with state of the art embedded receivers - P = position (3D RMS), V = velocity (3D RMS), T = timing (RMS). Autonomy is expressed in parameters upload per year. Robustness was expressed as the ranging error with a perturbation affecting the spacecraft (latch-up event, manoeuvre).

Technique	P [m]	V [mm/s]	T [ns]	Availability	Autonomy	Robustness
GNSS - Standalone [64] [45] [48] [74] p.19	1.5-15	30-500	10-40	0.995-0.999	TBD	100 m
DORIS - Standalone [11] [43]	1-5	0.3	3 000-5 000	0.995	15 (V1) , 0 (V2)	50 m
SLR	0.003-0.01	100	1 000	Unk., Low	0	Unk.

A trade-off analysis between the different navigation systems is presented in the following table. Table 2.3.1 shows that the GNSS standalone (i.e. a GNSS module is the only sensor onboard) has similar performance in position with DORIS. However, with respect to velocity accuracy, the performance of GNSS is 10 times lower than that of DORIS. The use of the GNSS clock delay solution provides approximately 100 times the accuracy of DORIS. SLR exceeds GNSS and DORIS positioning performance by a factor 100. SLR is slightly better than DORIS for timing accuracy, but worse than GNSS for timing accuracy. No sufficiently reliable figures have been found for the availability of SLR, but it may be lower than GNSS and DORIS due to the dense schedule of observatories and the variability of weather conditions. DORIS and GNSS availability are similar. Robustness was more difficult to evaluate. For GNSS, data was found for a latch-up event perturbation [40] (p.30). The receiver was used one orbit per day, leading to a 100 m accuracy. For DORIS, [43] indicates that the error during an apogee raising maneuver of 8 km, the error was about 50 m.

2.4 The IERS 2010 convention
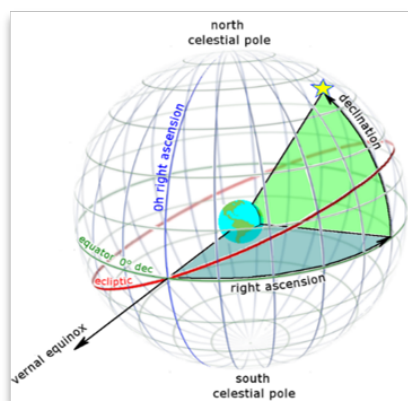
(a) GCRS (Geocentric Celestial Reference System)
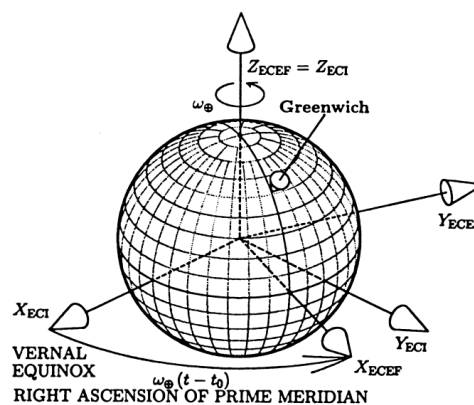
Fig. C.5 ECI and ECEF Coordinates.

(b) ECEF and ECI frames from [5]

Figure 2.4.1: Frames of the IERS convention

Celestial frames are non rotating and inertial frames. Terrestrial frames are used for navigation in the vicinity of the Earth. State of the art reference frames are defined and monitored by the IERS convention using SLR, DORIS, Very Long Baseline Interferometry (VLBI) and GNSS measurements. VLBI is a technique using the radio signals from extragalatic quasars. VLBI is used to define the inertial reference frame for navigation [75]. Fig. 2.4.1a shows Geocentric Celestial Reference Frame (GCRF) which is a non rotating ECI frame. The x-axis points toward the vernal equinox, the z-axis points towards the north celestial pole and the y-axis makes a right-handed frame. It is used for orbit propagation because it is quasi inertial (i.e. the residual

accelerations are very low). Fig. 2.4.1 show the relation between an ECEF frame rotating with the Earth. The origin is the Earth geocenter, the x-axis is the Greenwich meridian, the z-axis is the geographical north pole and the y-axis makes a right-handed frame. In the IERS 2010 convention, the ITRF is used and it is an ECEF frame. The conversion from the GCRF to ITRF requires intermediate frames. GCRF is converted to Celestial Intermediate Reference Frame (CIRF) with precession and nutation motion. CIRF is converted to Terrestrial Intermediate Reference frame (TIRF) using Earth rotation. Eventually, CIRF is converted to ITRF using polar motion. Fig. 2.4.2 illustrates the effects of precession nutation and polar motion of the rotation axis of the Earth.
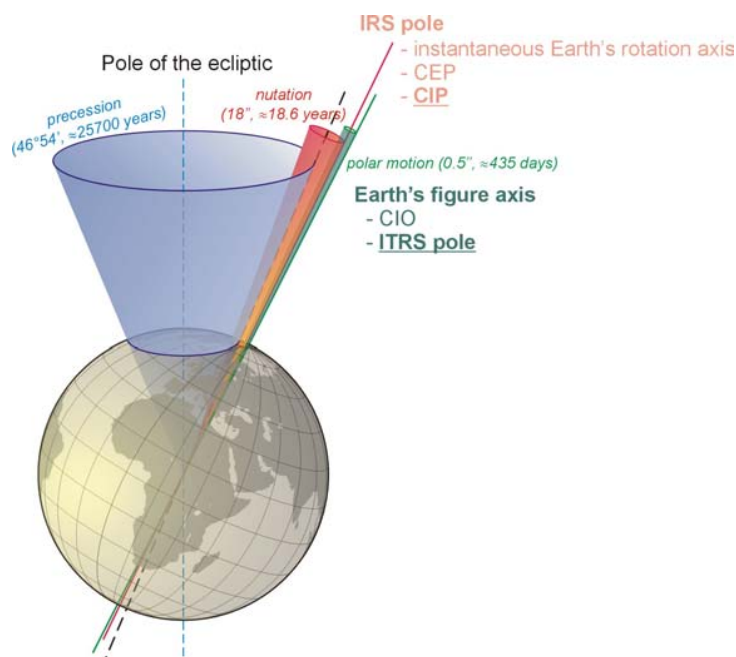
Figure 2.4.2: Phenomena impacting Earth rotation axis orientation, reprint with authorisation from Dr. J. Krynski [37]

Precession, nutation, Earth rotation angle and polar motion are described with the EOP. EOP are published in Bulletin A which is given weekly by the IERS at US Naval Observatory (USNO). Bulletin B/C04 is provided monthly by the IERS at the Paris Observatory. It provides daily data up to 30 days previous to the date of publication. Accuracies of each bulletin are limited and should be considered for the most precise applications [52].

2.4.1 Time systems

An *epoch* is an instant in time as determined by some singular event (e.g. the passage of a star across a meridian). A *clock* is a specification of epochs, given as a count of regular oscillations of a pendulum, from an agreed reference epoch. It can be a quartz crystal clock or an atomic clock. A *time system* is a set of standards agreed upon for naming epochs and synchronizing clocks.

- UT1: The Universal Time is a time standard based on Earth's rotation. At noon in UT1 time, the Sun is *on average* at zenith. Due to various phenomena (tidal forces from the Moon, the Sun, planets, oceans, atmosphere and gephysical effects like free-core nutation [55]), UT1 drifts over time. For IERS implementations with a higher accuracy, the tides due to Sun and Moon are accounted. Then UT1 is called the regularised UT1R.

- UTC: The Coordinated Universal Time a discontinuous time scale. It is based on the International Atomic Time (TAI), i.e. one TAI seconds is exactly one UTC second (approximation valid within $\sim$ 4 ns). Leaps seconds cause discontinuity, i.e. the UTC minute sometimes lasts 61 or 59 seconds. Only positive leap seconds have been introduced so far. It is theoretically possible to have negative leap seconds. EOP from Bulletin A are given every day at 0h00 UTC. Special care shall be taken during leap second days, because the duration of the day is 86 401 s (in case of a positive leap second). Leap seconds are not predictable, because some physical phenomena affecting UT1 remain unmodelled. UTC is valid only after 1972. The absolute difference between UTC and UT1 is kept within 0.9 s by adding leap seconds to UTC.

- GPS: The GPS time scale is an atomic time scale used by the GPS system to synchronise receivers. GPS is steered to mitigate the offset to UTC by 100 ns (apart from leap seconds). Other GNSS constellations have similar time systems, with an offset (eg. GGTO = GPS to Galileo Time Offset). To convert GPS to TAI, as of March, 27 2023:

$$\text{TAI} = \text{GPS} + 19s \tag{2.22}$$

- Terrestrial Time (TT): The Terrestrial Time is an astronomical time standard defined by the International Astronomical Union. In the following, the approximation TT = TDT (Terrestrial Dynamical time) = ET (Ephemeris time) was adopted. It is valid within a few nanoseconds. TT is linked to TAI by :

$$\text{TT} = \text{TAI} + 32.184s \tag{2.23}$$

- TAI: International Atomic Time (*Temps Atomique International* in French) is a high-precision atomic coordinate time standard. It is 5 orders of magnitude more stable than UT1. It is based on 380 atomic clocks, in 70 laboratories across the globe. It is maintained by the *Bureau International des Poids et Mesures* in France.

Fig. 2.4.3 shows the links between each time system. Δ A is the number of leap seconds at time of application. It is represented by a step function. UT1-UTC and TAI-UT1 are continuous functions, the values f(t) and g(t) are not predictable and need and external source to be
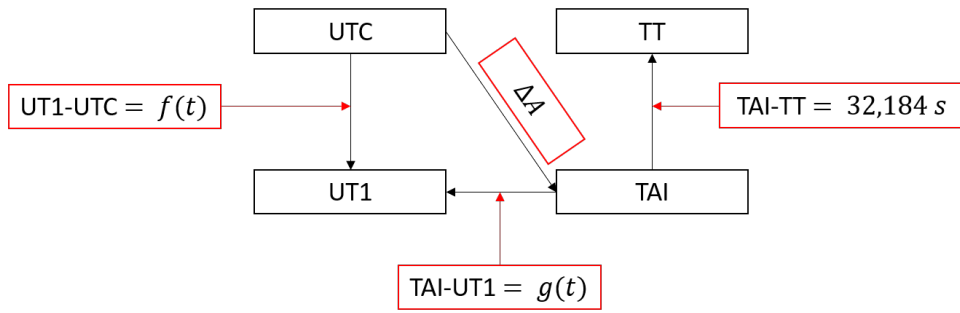
Figure 2.4.3: Time systems conversions

estimated. The TT - TAI difference is constant (32.184 s). The UTC-TT is a discontinuous step function :

$$UTC - TT = UTC - TAI + TAI - TT = -Ls - 32.184s \qquad (2.24)$$

.

As an example, before UTC 2005-12-31 23:59:59 (included), the number of leap seconds is 32 so the UTC - TT difference would be -32 - 32.184 = - 64.184 s.

Two epochs are given as an example. It corresponds to the 33 rd leap second introduced in the UTC time scale. UTC 2005-12-31 23:59:59 is represented in TT as 2006-01-01 00:01:03.184. UTC 2005-12-31 23:59:60 is represented in TT as 2006-01-01 00:01:04.184. The offsets between time systems versus time is represented in Fig.2.4.4
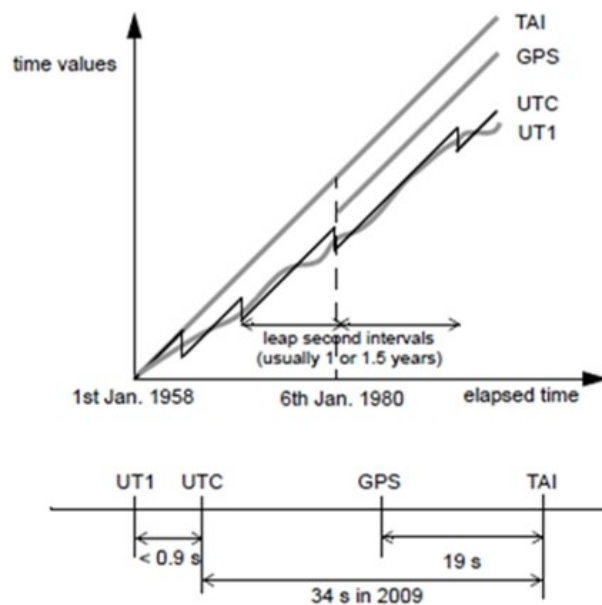
Figure 2.4.4: TAI, UT1, UTC and GPS time systems

2.4.2 Frame conversion

The frame conversion between an ECI and an ECEF frame is often overlooked. In the less accurate applications, only the Earth's rotation angle parameter needs to be used, which leads to a 3D RMS accuracy of about 46-90 km [8]. A preliminary visibility analysis of GNSS constellations may comply with this accuracy. For AOCS purposes of precise navigation, such a simplification is not acceptable. On the other hand, the full implementation of the IERS convention (refered as the *Full theory*) is very cumbersome for on-Board implementation (the precession nutation parameters require about 4000 coefficients). The equinox-based method and the Celestial Intermediate Origin (CIO) based method are presented in Fig. 2.4.5. Basically, the CIO is the x-axis of the Celestial Intermediate Reference Frame [53] (p. 47). The method differs from the equinox in that it uses Earth Orientation parameters. Both methods implement the convention with similar accuracies, but the CIO method is preferred due to the higher availability of the parameters to implement the method. Thus, the equinox based method will not be discussed. There are three procedures : the *Full theory*, the series and the interpolation. The Series method was investigated in Chapter 4. Bradley [8] showed that this procedure yields good accuracy with limited computational requirements.
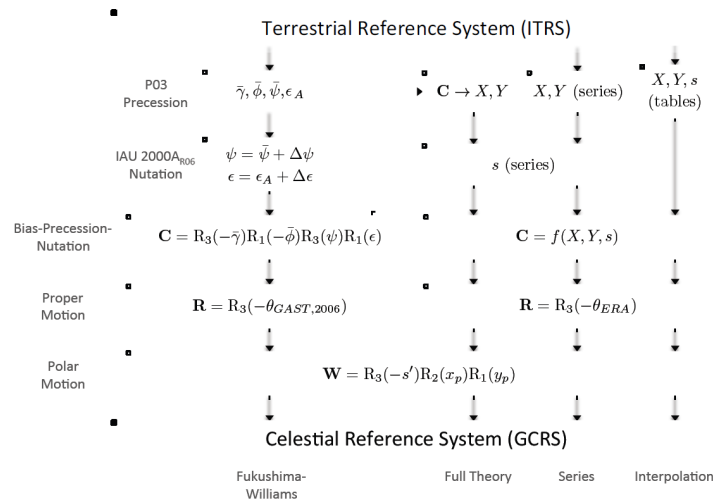
Figure 2.4.5: Full theory

The frame transformation is used to convert a vector expressed in GCRF frame coordinates to ITRF frame coordinates. This transformation is defined as:

$$\mathbf{T} = [\mathbf{Q}(X, Y, s)] \, [\mathbf{R}(\text{ERA})] \, [\mathbf{W}(x_p, y_p, s')] \tag{2.25}$$

[$\mathbf{Q}$] is the bias-precession-nutation matrix. [$\mathbf{R}$] is the Earth rotation matrix and [$\mathbf{W}$] is the polar motion matrix. The parameters X, Y describe the precession angles. Parameter s is the CIO locator, it describes the nutation. Earth Rotation angle (ERA) represents the proper

rotation of the Earth around it's instantaneous rotation axis. x_p, y_p and s' are the polar motion components. The ITRF (International Terrestrial Reference Frame) is an ECEF frame, i.e. rotating with the Earth. There are several intermediate frames. The polar motion matrix $\mathbf{W}$ converts the ITRS to the Terrestrial Intermediate Reference System (TIRS). It is computed with the polar motion parameters (x_p,y_p). Corrections on the polar motion parameters are provided in [53]. Ocean tides were neglected in the implementation, so the polar motion components provided by the IERS were used directly.

R_1,R_2,R_3 denote the Direction Cosine Matrices with a rotation along axis 1,2 and 3.

$$
\begin{aligned}
t &= (\text{TT}_{\text{JD}} - 2400000.5)/36525 & \text{(Jcy of TT)} \\
s' &= -47\mu\text{as} \cdot t & \text{(TIO locator)} \\
[\mathbf{W}] &= [R_3(-s')]\,[R_2(x_p)]\,[R_1(y_p)] & \text{(Polar motion matrix)}
\end{aligned}
\tag{2.26}
$$

$$
\mathbf{r}_{\text{TIRS}} = [\mathbf{W}]\,\mathbf{r}_{\text{ITRS}}
\tag{2.27}
$$

The Earth rotation matrix $[\mathbf{R}]$ converts the TIRS to the Celestial Intermediate Reference System (CIRS).

$$
\begin{aligned}
\text{UT1}_{\text{JD}} &= \text{TAI}_{\text{JD}} - (\text{TAI-UT1})/86400 \\
\text{T}_u &= \text{UT1}_{\text{JD}} - 2451545.0 \\
ERA &= 2\pi\left(\text{mod}(\text{UTC}_{\text{JD}}, 1) + 0.7790572732640 + 0.00273781191135448 \cdot \text{T}_u\right)
\end{aligned}
\tag{2.28}
$$

$$
\mathbf{r}_{\text{CIRS}} = [\mathbf{R}]\,\mathbf{r}_{\text{TIRS}}
\tag{2.29}
$$

The bias-precession-nutation $[\mathbf{Q}]$ is defined with the precession nutation components X & Y. Those parameters were computed using the truncated series method. This method uses polynomial approximation of X and Y, selecting the dominant coefficients. This method has a high accuracy and a reduced computation cost. The nutation coefficients (F, D, Ω) are computed with the parameter $t = $ Julian centuries of TT, where TT is expressed as Julian days. t is defined according to (2.30):

$$
t = \frac{\text{TT}_{\text{JD}} - 2\,400\,000.5}{36\,525}
\tag{2.30}
$$

Affine approximations were used to compute the nutation coefficients (l, l', F, D, Ω). Only F, D, Ω were used. They are given as radians in the following formula.

$$
\begin{aligned}
F &= 1.6279050815 + 8433.4661569164 \cdot t \\
D &= 5.1984665887 + 7771.3771455937 \cdot t \\
\Omega &= 2.1824391966 - 33.7570459536 \cdot t
\end{aligned}
\tag{2.31}
$$

The more coefficients are used to compute X and Y, the more precise the precession. It also requires to store the coefficients On-Board.

- 4 coefficients series (given in arcseconds [as]) :

$$
\begin{aligned}
X(t) &= 2004.191898 \cdot t - 6.844318 \cdot \sin(\Omega) \\
Y(t) &= -22.407275 \cdot t^2 + 9.205236 \cdot \cos(\Omega)
\end{aligned}
$$

- 6 coefficients series :

$$
\begin{aligned}
X(t) &= 2004.191898 \cdot t - 6.844318 \cdot \sin(\Omega) - 0.523908 \cdot \sin(2F - 2D + 2\Omega) \\
Y(t) &= -22.407275 \cdot t^2 + 9.205236 \cdot \cos(\Omega) + 0.573033 \cdot \cos(2F - 2D + 2\Omega)
\end{aligned}
$$

- 15 coefficients series :

$$
\begin{aligned}
X(t) &= -0.016617 + 2004.191898 \cdot t - 0.429783 \cdot t^2 - 6.844318 \cdot \sin(\Omega) \\
&\quad + 0.082169 \cdot \sin(2\Omega) - 0.090552 \cdot \sin(2F + 2\Omega) - 0.523908 \cdot \sin(2F - 2D + 2\Omega) \\
&\quad + 0.205833 \cdot t \cdot \cos(\Omega) \\
Y(t) &= -0.025896 \cdot t - 22.407275 \cdot t^2 + 9.205236 \cdot \cos(\Omega) \\
&\quad - 0.089618 \cdot \cos(2\Omega) + 0.097847 \cos(2F + 2\Omega) + 0.573033 \cdot \cos(2F - 2D + 2\Omega) \\
&\quad + 0.153042 \cdot t \cdot \sin(\Omega)
\end{aligned}
$$

The precedent computations are derived from the model of torques acting on the Earth, changing its instantaneous momentum of rotation. The model is not perfect thus there are small offsets to the measured value of the precession and nutation angles. These offsets are measured with VLBI technics and provided in the IERS EOP [71]. The celestial pole offsets amplitude dX and dY are a few mas and were disregarded in the computation of X and Y.

$$
a = \frac{1}{2} + \frac{1}{8}\left(X^2 + Y^2\right)
\tag{2.32}
$$

$$
Q(t) = \begin{pmatrix}
1 - aX^2 & -aXY & X \\
-aXY & 1 - aY^2 & Y \\
-X & -Y & 1 - a\left(X^2 + Y^2\right)
\end{pmatrix} \cdot R_3(s)
\tag{2.33}
$$

$$R_3(s) = \begin{pmatrix} \cos(s) & \sin(s) & 0 \\ -\sin(s) & \cos(s) & 0 \\ 0 & 0 & 1 \end{pmatrix} \qquad (2.34)$$

Eq. 2.34 describes the rotation associated to the CIO locator s. In the following, s was set to 0 thus R_3(s) = I_3.

$$s = -XY/2 \qquad (2.35)$$

Eq. 2.35 is a simplification. There are other terms analogous to X and Y. They were neglected, and the approximation holds to 6 mas (or 1.6×10^{-6} rad). [72] (p. 281)

The bias-precession-nutation matrix $[\mathbf{Q}]$ relates the CIRS to the GCRS.

$$\mathbf{r}_{\text{GCRS}} = [\mathbf{Q}]\, \mathbf{r}_{\text{CIRS}} \qquad (2.36)$$

To convert from position vector in ITRF frame coordinates, the following transformations shall be used [9] [38]. The contribution of $\dot{\omega}$ was disregarded ($-\dot{\omega} \times \mathbf{r}$). Also the contributions of time derivatives of $[\mathbf{Q}]$, $[\mathbf{R}]$ and $[\mathbf{W}]$ were disregarded.

$$
\begin{aligned}
\mathbf{r}_{\text{GCRF}} &= [\mathbf{Q}]\,[\mathbf{R}]\,[\mathbf{W}]\, \mathbf{r}_{\text{ITRF}} \\
\mathbf{v}_{\text{GCRF}} &= [\mathbf{Q}]\,[\mathbf{R}]\, ([\mathbf{W}]\, \mathbf{v}_{\text{ITRF}} + \omega \times \mathbf{r}_{\text{ITRF}}) \\
\mathbf{a}_{\text{GCRF}} &= [\mathbf{Q}]\,[\mathbf{R}]\, ([\mathbf{W}]\, \mathbf{a}_{\text{ITRF}} + \omega \times \omega \times \mathbf{r}_{\text{ITRF}} + 2\omega \times \mathbf{v}_{\text{ITRF}})
\end{aligned}
\qquad (2.37)
$$

With the Earth rotation vector

$$\omega = \begin{bmatrix} 0 & 0 & \omega_\oplus \cdot \left(1 - \dfrac{\text{LOD}[s]}{86400}\right) \end{bmatrix}^{\text{T}} \qquad (2.38)$$

and the nominal Earth rotation rate, consistent with the IERS 2010 convention :

$$\omega_\oplus = 7.292\,415 \times 10^{-5} \text{rad/s} \qquad (2.39)$$

The orbit propagation requires the knowledge of the forces expressed in an inertial frame. This is done by applying the transformation $[\mathbf{Q}]\,[\mathbf{R}]\,[\mathbf{W}]$. Montenbruck [50] and Bradley [9] have studied the possibility of propagating the orbit in the ITRF frame. If an Inertial Measurement Unit (IMU) is used, accelerations and velocities are expressed in the body frame. Once

accelerations and velocities are converted to the terrestrial frame, Eq. 2.37 can be used to convert them to the GCRF frame and propagate the orbit.

Chapter 3

Contributions to the onboard navigation software

The following chapter describes the contributions to the onboard navigation software during the internship. The details of the EOP analysis implementation and time system conversions are described. The validation process with data from *Observatory of Weights and Measures of Paris* and simulated orbits with the propagator of reference is explained. Fig. **??** shows a high-level explanation of the work.

3.1 Earth Orientation Parameters

EOPs were retrieved and analysed using IERS data. Typical values, evolution over time and uncertainties are presented in the following paragraphs.
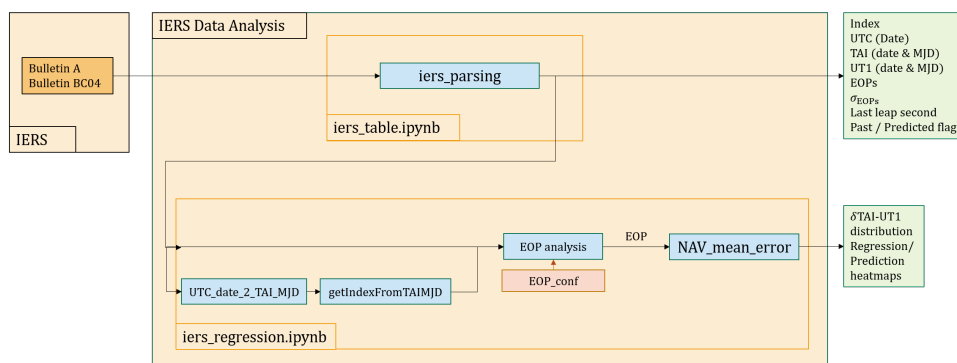
Figure 3.1.1: EOP analysis

- TAI-UT1 (s) : describes the time difference between the TAI time scale and UT1 time scale (Fig. 3.1.3, see Background Section). It is used to compute retrieve UT1 from TAI. UT1 is

used to compute the Earth rotation angle (ERA). TAI - UT1 is also used.

$$UT1 = TAI - (TAI - UT1) \tag{3.1}$$
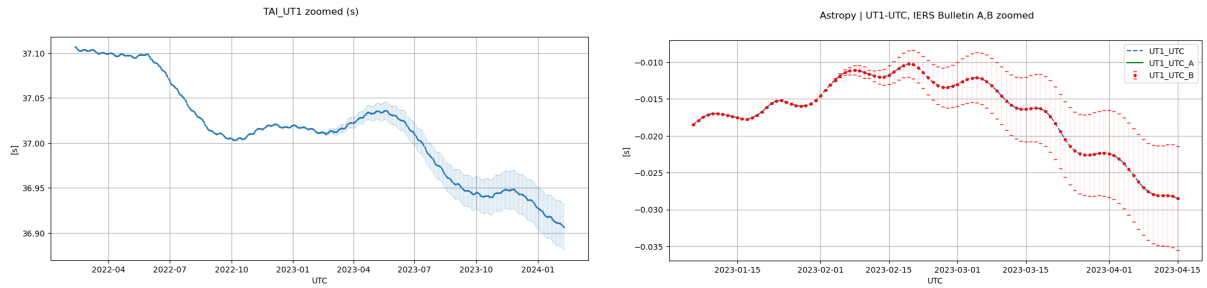
(a) TAI-UT1 as of January 2023, $\pm 1\,\sigma$ (Bulletin A)   (b) UT1-UTC as of January 2023, $\pm 1\,\sigma$ (Bulletin A)

Figure 3.1.2: TAI-UT1 & UT1-UTC, Bulletin A
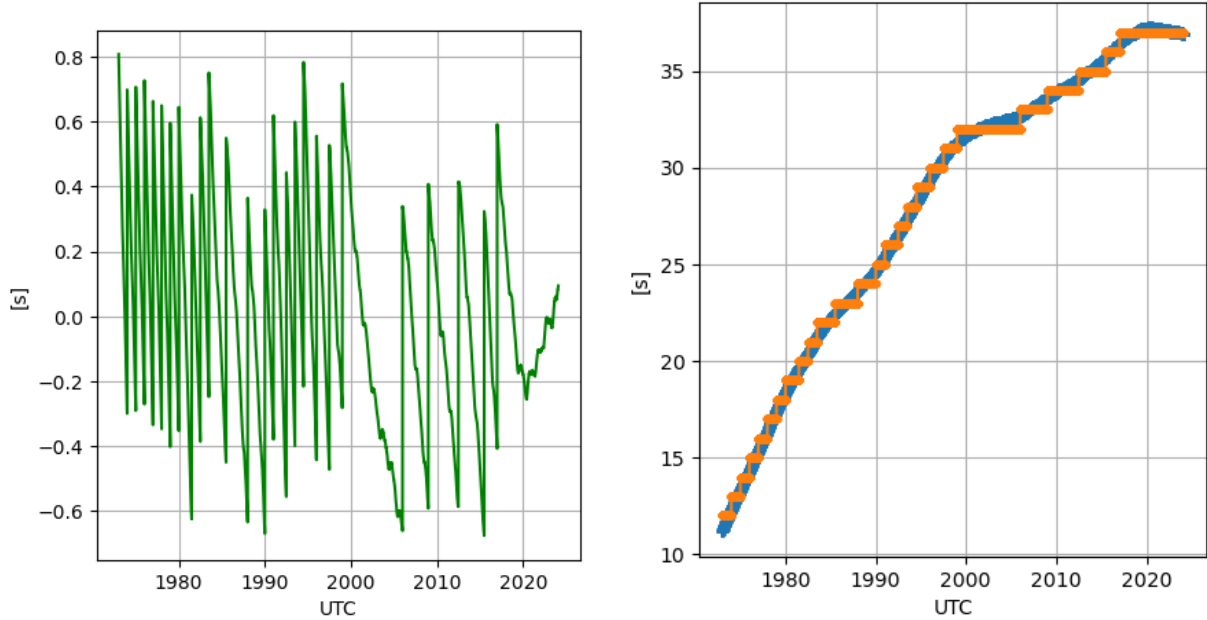
(a) TAI-UT1   (b) TAI-UTC (step), TAI-UT1 (continuous)

Figure 3.1.3: Left: UT1-UTC, Right: TAI-UTC & TAI-UT1

- x_p, y_p (as) : polar motion x-component. The motion is described with respect to the instantaneous Earth rotation axis, in the TIRF.

(a) Polar motion vs. time   (b) Polar motion in XY plane
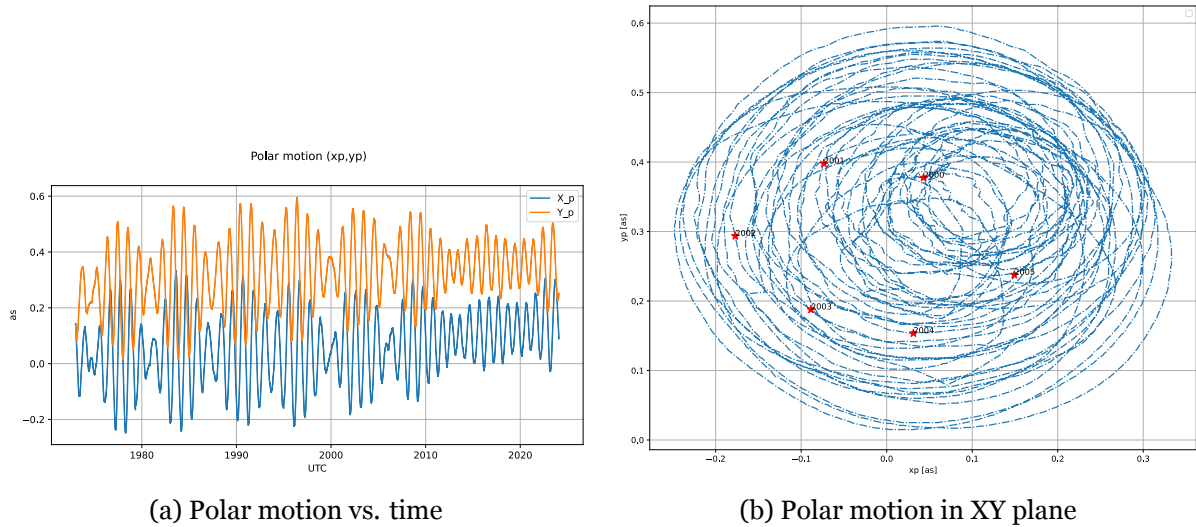
Figure 3.1.4: Polar motion

- dX, dY (mas) : Celestial Pole offset, x and y components. This parameter is obtained from observations.
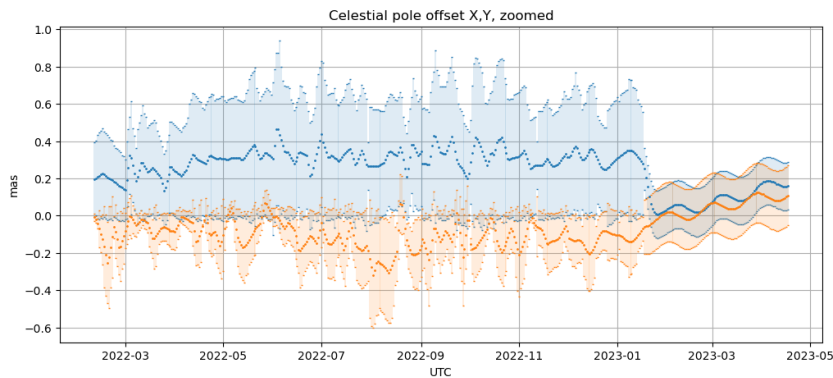
Figure 3.1.5: Celestial Pole Offset, measured and predicted values (up to January 2023) and predicted values, $\pm\,1\,\sigma$ (Bulletin A)

- LOD (ms) : describes the excess of duration of a UT1 day with respect to the nominal duration of a Julian day (86400 s). It is used to determine the instantaneous rotation vector of the Earth.

Figure 3.1.4 shows the time evolution of the polar motion with it's XY plane representation in Figure 3.1.4b. The effect is typically a few arcseconds and contributes to 10-20 meters in the frame conversion accuracy [8]. The accuracy of past polar motion parameter given by the IERS is typically 42 μas, with 30 μas precision. [52] Due to the presence of tidal forces and gravitational pulls from other bodies in the solar system, the duration of a sidereal day is not constant. Figure 3.1.6 shows the excess of duration with respect to the nominal duration of 86400 s.

The CIO based method was used, implementing the IERS 2010 convention. The CIO method
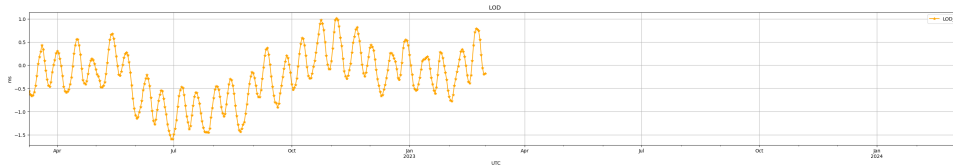
Figure 3.1.6: Offset to nominal Length of Day (86400 s)

[30] breakdowns the conversion from ITRF to GRCF in several components : a frame bias, precession and nutation and polar motion. The conventional reference implementation is referred as the *Full Theory*. This method is quite cumbersome, it considers effects such as tidal forces and libration and the precession nutation coefficients computation involves up to four thousands of coefficients. The precession nutation parameters can be approximated with the truncated series. A 15th coefficients approximation results in a 30 mas accuracy which is usually sufficient [73] [72] [13]. EOPs are given by the IERS each day at 0h00 UTC.

Table 3.1.1: Frame 3D RMS error associated to each EOP [8]. Error at a representative altitude of 800 km.

Case	Error	EOP included in work ?
GMST only	~ 27 km	X (ERA instead)
Δ UT1 = 0 s	~ 350 m	✓(UT1 yields ERA)
Polar motion (x_p,y_p) = 0	~ 20 m	✓
Ocean tide	~ 6 cm	X (Neglected)
Celestial Pole offset (dX,dY) = 0	~ 4.5 cm	X (Neglected)
Single value Julian day	~ 2.9 cm	X (Double values)
Zonal tides (ΔUT1R)	~ 17 mm	X (Neglected)
Libration effect	~ 1 mm	X (Neglected)

3.2   Library implementation

The section describes the Data analysis libraries implemented during the internship. Notebooks were developed for automatic reports. Data download from IERS servers was configured to update automatically to ensure the latest data is available. A set of libraries was developed and validated to perform frame conversions and time system conversions. A full description of inputs and outputs can be found in the Annex.

3.2.1 Time systems conversion

Routines to convert UTC to TAI, TT and UT1 were validated using the a reference astrodynamics library. The expected values and results are listed in the following table. The following paragraph details the implementation of the time scale conversion.

- UTC $\longrightarrow$ TAI : the transformation is exact. First the UTC date is converted to an internal format using the date2string function. Then the date part of UTC is extracted and converted to TAI MJD. This allows to find the correct row in the IERS table and retrieve the correct TAI-UTC value. The conversion was validated over an epoch corresponding to a UTC leap second.

- UTC $\longrightarrow$ TT : The transformation is exact. The process is the same as for UTC $\longrightarrow$ TAI. First UTC is converted to TAI using the precedent UTC $\longrightarrow$ TAI. Then a simple timedelta is applied to TAI to find TT.

- UTC $\longrightarrow$ UT1 : The transformation is approximate. A 100 µs accuracy was achieved. UTC is converted to TAI in a first time. Then the TAI $\longrightarrow$ UT1 method (described below is used).

- TAI $\longrightarrow$ UT1 : The transformation is approximate. A 100 µs accuracy was achieved. First, the latest 0h00 UTC epoch is found and expressed as TAI MJD. The routines were used to estimate the TAI-UT1 at any epoch between two 0h00 UTC epochs.

3.3 Validation

The frame conversion method was validation against two independent sources of data. The bias-precession-nutation coefficients were computed using a 15 terms truncated series (see Background section).

3.3.1 Reference space mechanics library

Several orbits were simulated with an orbit propagator. Selected altitudes were LEO 800 km, GPS 20200 km, and GEO 36000 km. Equatorial orbits, polar and SSO orbits were simulated. The models used for the propagation of the orbit were described in the Method Section. The inertial coordinates were expressed in GCRF and propagated by the propagator of reference in the GCRF frame. The propagator of reference implements the IERS convention with rotational errors of about µas and was validated against in-flight data of the ATV. Thus, propagated GRCF coordinates could be converted to ITRF coordinates. The propagated GCRF coordinates were given as an input of the libraries developed during the intership. The output ITRF coordinates

and velocities were compared agaisnt reference ITRF coordinates. Fig. 3.3.1 summarize this conversion:
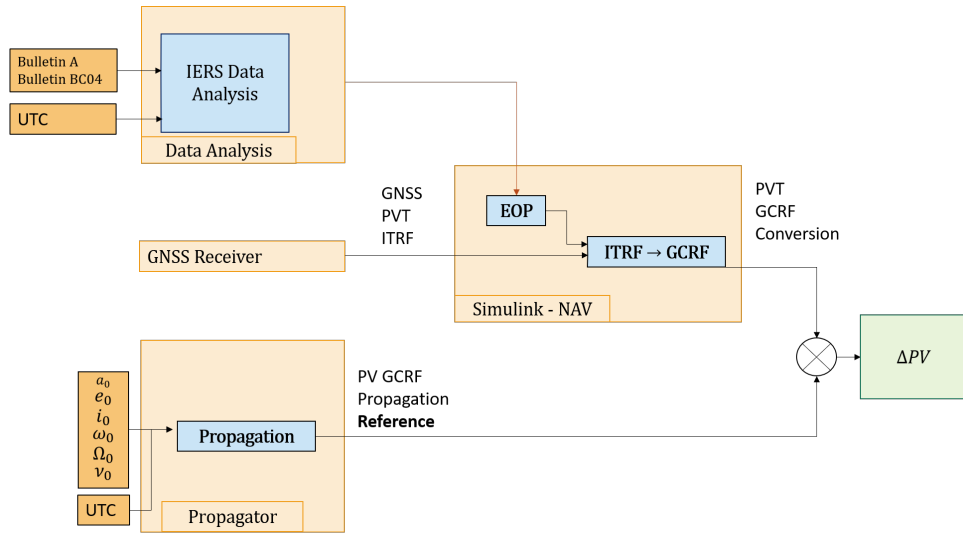
Figure 3.3.1: Validation of data analysis implementation of simplified ITRF/GCRF conversion with reference space mechanics library
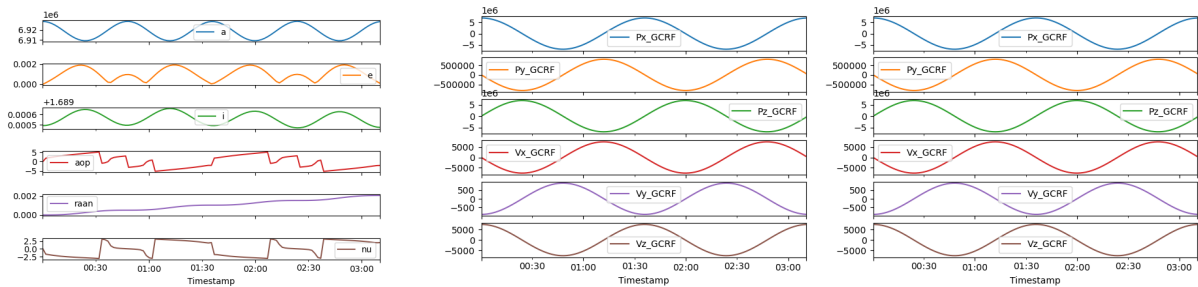
(a) Propagated orbit elements. (b) Spacecraft ITRF coordinates (c) Spacecraft GCRF coordinates

Figure 3.3.2: Propagated keplerian orbit in different coordinates systems. Semi-major axis and cartesian coordinates in m. Angles in radians, velocities in m/s. Elements are : semi major axis, eccentricity, inclination, argument of perigee, RAAN, true anomaly

The validation with the propagator of reference allowed some tuning of the method. The effect of truncated series on nutation/precession was assessed. The effect of using the CIO locator and linearised rotation matrices was estimated. Note that the propagation errors did not influence the validity of the process. Both the reference data and the coordinates converted to the ITRF frame were propagated. A simulation of 900 orbits in LEO at 800 km altitude was run. The simulation period extends over two months, from 2010-10-01 to 2010-12-01 UTC. Fig. 3.3.3a shows the 3D error in ITRF coordinates. The reference inertial coordinates propagated in the inertial GCRF frame were converted to ITRF. TAI-UT1 and polar motion components were predicted over two months . As expected, the general trend is a linear drift with increasing deviation. The linear drift is about 0.25 m/day in the worst case scenario. A similar work over the period 2018-10-01 → 2018-12-11. It shows an initial decrease of the error (see Fig. 3.3.3b).

Fig. 3.3.3a shows the worst case observed. i.e. a linear drift of the error over time. According to Table 2.1.5, an accuracy of 5-15 m could be achieved with a COTS single frequency GNSS receiver. Fig. 3.3.3a shows that a 5 m 3D error was achieved after 15 days of propagation. It suggests the update could be done every two weeks to mitigate the error.

(a) Frame bias arising from IERS 2010 implementation. Reference Data from propagator. y-axis in meter.

(b) Frame bias arising from IERS 2010 implementation in data analysis. 200 orbits simulated over the period 2022-12-09 to 2022-12-21.y-axis in meter.
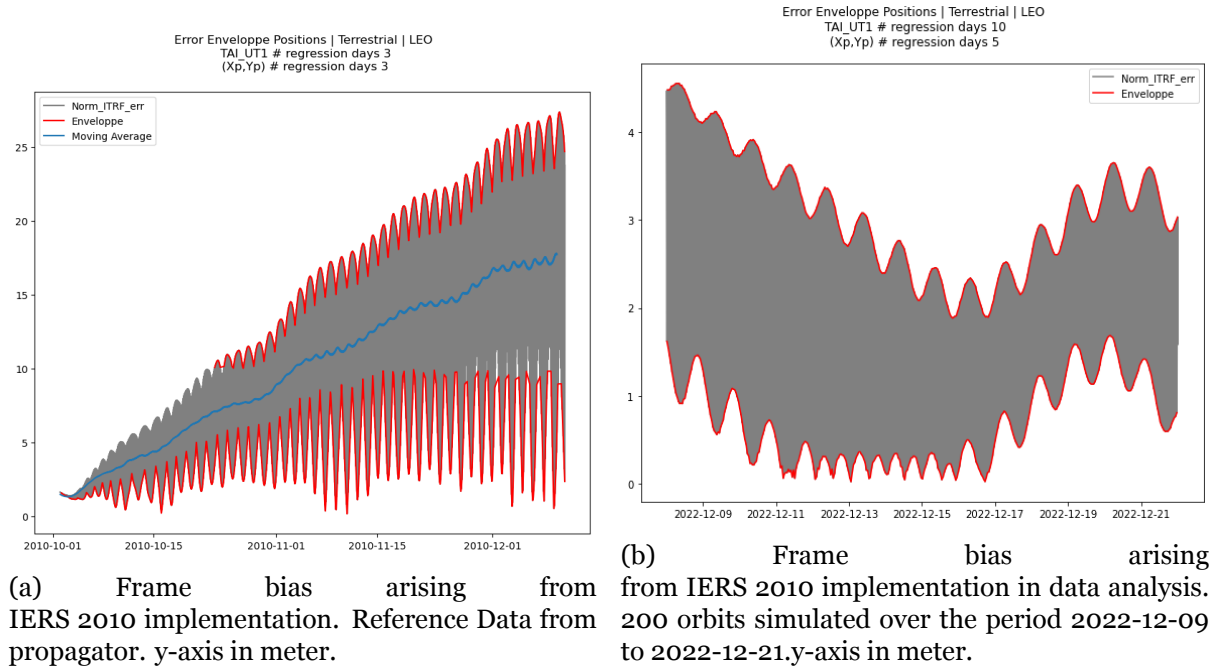
Figure 3.3.3: Frame bias arising from IERS 2010 implementation in data analysis.

Fig. 3.3.5 shows a breakdown of velocity components errors and the 3D error. Eq. 2.37 was used to convert a velocity $\mathbf{v}_{\mathrm{ITRF}}$ to $\mathbf{v}_{\mathrm{GCRF}}$. The reference data is the inertial velocity $\mathbf{v}_{\mathrm{GCRF}}$. After 60 days, the velocity 3D error is less than 0.8 mm/s. According to Table 2.3.1, GNSS has a 3D RMS accuracy of 30 to 500 mm/s. The performance achieved by the frame conversion is better. Thus, the frame conversion should have a relatively low impact in the error budget.

3.3.2 Validation with data from Observatoire des Poids et mesures de Paris

The *Observatoire des Poids et mesures de Paris* provides a tool [54] to compute the rotation matrices $[\mathbf{Q}],[\mathbf{R}],[\mathbf{W}],[\mathbf{T}]$ over a given period. Two periods were investigated, with a sampling rate of 1 day.

- Period 1 : January 2000 - February 2000

- Period 2 : January 1995 - January 2022

The input data was indexed with MJD TAI. The components of the bias-precession-nutation, earth rotation and polar motion matrices were provided on each column. The rotational error (as defined in Method section) was computed for each matrix. The resulting position error

in LEO (defined in Method section) was derived for the X,Y,Z components and the RSS 3D error as well. The reference data was computed by *Observatoire des Poids et mesures de Paris* with the Full Theory method. It was compared against the simplified method. The results are shown in the following tables.Fig. 3.3.6a suggests that the maximum error associated to the bias-precession-nutation transformation over a month is 4.0 m. It is comparable to the results of Bradley [8] who retrieved a maximum error of 4.8 m over 60 years with one value each day. For the Earth rotation transformation, the maximum error is 0.055 m and for the polar motion the maximum error is 0.032 m.

(a) Bias-precession-nutation

(b) Earth rotation error

(c) Polar motion error

Figure 3.3.4: Error breakdown arising from bias-precession-nutation transformation [$\mathbf{Q}$], Earth rotation transformation [$\mathbf{R}$], polar motion transformation [$\mathbf{W}$] over Period 1, Reference data from *Observatoire des Poids et Mesures de Paris*

Table 3.3.1: Errors over Period 1. See Method section for error definition.

Matrix	Rotational error [rad]	dx [m]	dy [m]	dz [m]	3D [m]
Q	2.12×10^{-6}	1.251	0.632	1.535	2.175
R	8.22×10^{-8}	0.019	0.019	0.000	0.0269
W	4.10×10^{-8}	0.0103	0.0045	0.0119	0.0169
T	2.12×10^{-6}	0.726	1.267	1.544	2.189

Results from Table 3.3.2 show that the main contributor to the frame error is the bias-precession-nutation matrix $\mathbf{Q}$. Errors were averaged over the selected period. Position errors were expressed at a representative 800 km altitude above a spherical Earth. Reference data from *Observatory of Weights and Measures of Paris*. X,Y components were computed using 15 terms truncated series. The TIO locator s was not included. Another period was selected to test the implementation over leap second. The test period is December 25th, 2005 to January 3rd, 2006. In Fig. 3.3.5a, the query sent to *Observatory of Weights and Measures of Paris* was January 1st 2006 UTC to January 3rd 2006 UTC. In Fig. 3.3.5b, the selected period was December 25th 2005 UTC to January 3rd 2006 UTC. The decimal part of the TAI MJD index does *not* correspond over the January 1st 2006 UTC to January 3rd 2006 UTC epochs. The shift value is 1/86400 s because of the leap second. There is a bias because on a positive leap

second days, the duration of a day is 86401 s. Thus the decimal part of MJD TAI is shifted by 1/86400 s. Thus, the data from this source is valid for EOP analysis only over periods without leap seconds.

```
                                       //          Civil date UTC         // Matrix
                       //          Civil date UTC      /   MJD TAI      / year / month / day / hour / min / sec /  R11 /
                                                           53729.000370370370 2005 12 25  0  0  0.0000000 -0.06153475170145 -
MJD TAI        / year / month / day / hour / min / sec     53730.000370370370 2005 12 26  0  0  0.0000000 -0.07869431376826 -
53736.000381944446 2006  1  1  0  0  0.0000000 -0.18105751   53731.000370370370 2005 12 27  0  0  0.0000000 -0.09583060430509 -
53737.000381944446 2006  1  2  0  0  0.0000000 -0.19794774   53732.000370370370 2005 12 28  0  0  0.0000000 -0.11293854964259 -
53738.000381944446 2006  1  3  0  0  0.0000000 -0.21477938   53733.000370370370 2005 12 29  0  0  0.0000000 -0.13001309609977 -
                                                           53734.000370370370 2005 12 30  0  0  0.0000000 -0.14704918240438 -
                                                           53735.000370370370 2005 12 31  0  0  0.0000000 -0.16404176160841 -
                                                           53736.000370370370 2006  1  1  0  0  0.0000000 -0.18105751570004 -
                                                           53737.000370370370 2006  1  2  0  0  0.0000000 -0.19794774668205 -
                                                           53738.000370370370 2006  1  3  0  0  0.0000000 -0.21477938348805 -
```

(a) Correct indexing in *Observatoire des Poids et mesures de Paris*

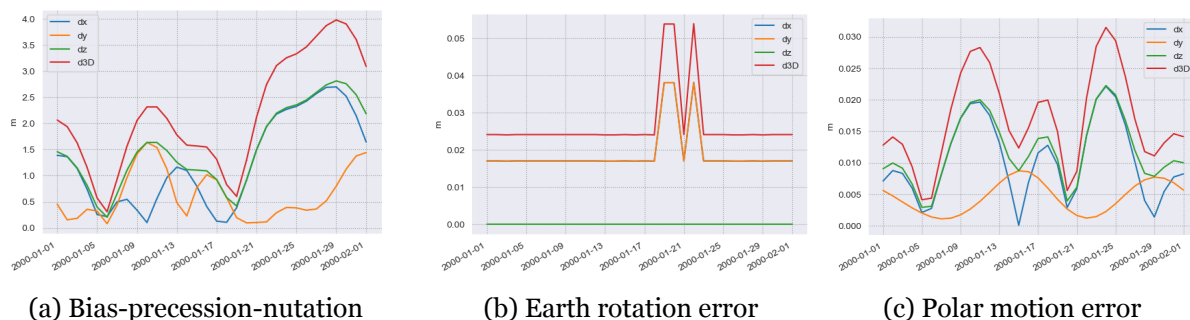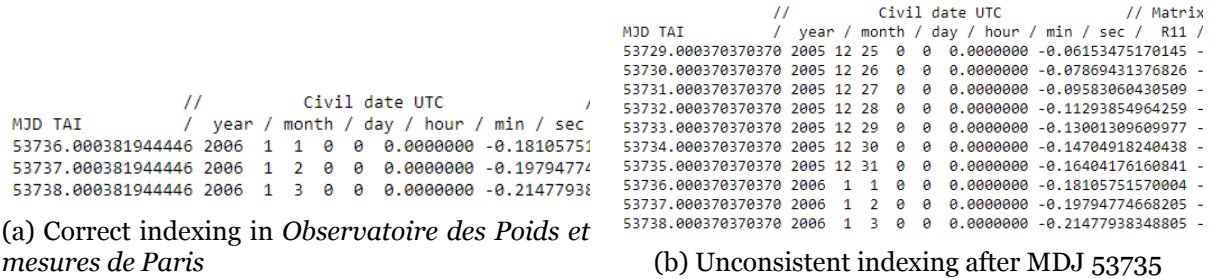(b) Unconsistent indexing after MDJ 53735

Figure 3.3.5: Error breakdown arising from bias-precession-nutation transformation [**Q**], Earth rotation transformation [**R**], polar motion transformation [**W**] over Period 1, Reference data from *Observatoire des Poids et Mesures de Paris*

(a) Bias-precession-nutation

(b) Earth rotation error
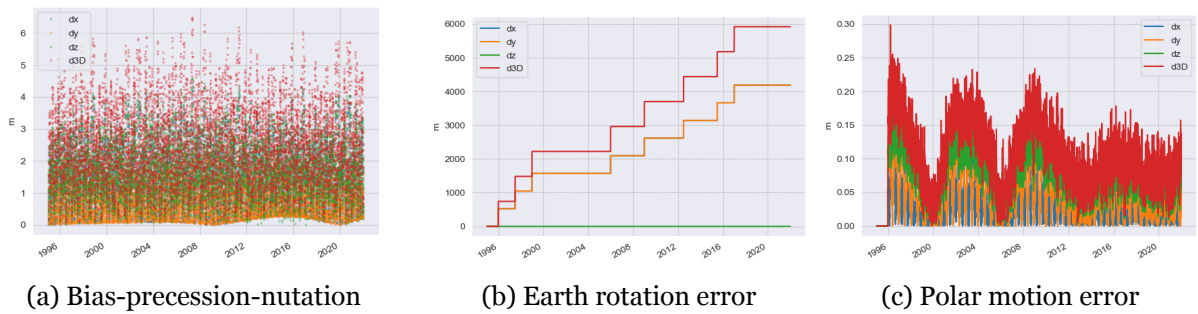
(c) Polar motion error

Figure 3.3.6: Error breakdown arising from bias-precession-nutation transformation [**Q**], Earth rotation transformation [**R**], polar motion transformation [**W**] over Period 2, Reference data from *Observatoire des Poids et Mesures de Paris*

Table 3.3.2: Errors over Period 2. Errors were averaged and expressed for a representative altitude of 800 km. Reference data from *Observatoire des Poids et Mesures de Paris*

Matrix	Rotational error [rad]	dx [m]	dy [m]	dz [m]	3D [m]
Q	2.35×10^{-7}	1.385	0.798	1.688	2.398
R	9.705×10^{-4}	2394	2394	0.0	3386
W	1.2×10^{-9}	0.049	0.045	0.074	0.105
T	9.705×10^{-4}	2395	2395	1.689	3387

Fig 3.3.6 shows the error is zero on z axis. The Earth rotation matrix is a rotation about z axis so this was expected. There were eight leap seconds over the period 1995-2020. TAI is normally *not* affected by leap seconds, but due to the incorrect indexing, the TAI in the index is off by 8 s. TAI is one of the input of the method implemented, and TAI was used to estimate UT1. Thus, UT1 was off 8 s as well. This results in a 2D error of 3386 m, or 423 m bias for each UT1 s bias.

In conclusion, it was possible to validate the whole implementation with a 3D RMS accuracy of 2 m over Period 1. It was also possible to validate polar motion and precession nutation over Period 2. However, the Earth rotation could not be validated as a bias was present in the data. The error is 423.4 m for each leap second, which is comparable to the linear speed at Earth surface at equator (464 m/s) [5] within 10%. Another analysis, performed in [20], compared of the truncated method versus the interpolation method. In the reference articles the truncature method was shown to contribute up to $\simeq$ 10 µm in the GCRS coordinates error so it can be used safely.

3.4 Cross validation : Reference propagator - Navigator

The same configuration was chosen for all the validation methods : 15 terms truncated series, no CIO locator, estimation of TAI-UT1 and polar motion components. The reference data is the propagated orbit. Fig. 3.4.1b and Fig. 3.4.2 show the 3D position error is less than 2.5 m and the velocity error
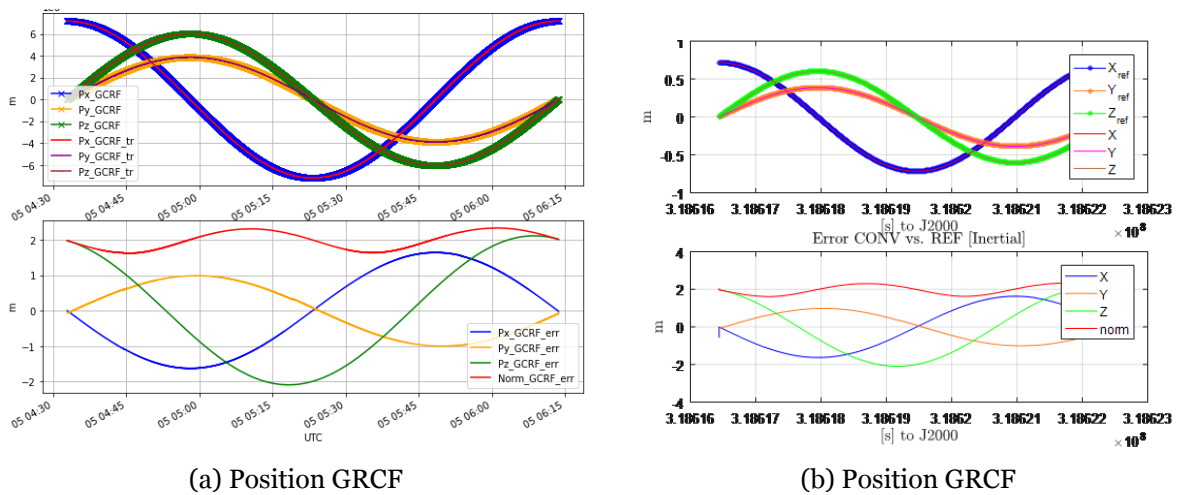

(a) Position GRCF

(b) Position GRCF

Figure 3.4.1: LEO - GCRF coordinates, absolute (top), error (bottom). Optimal scenario with unbiased EOPs

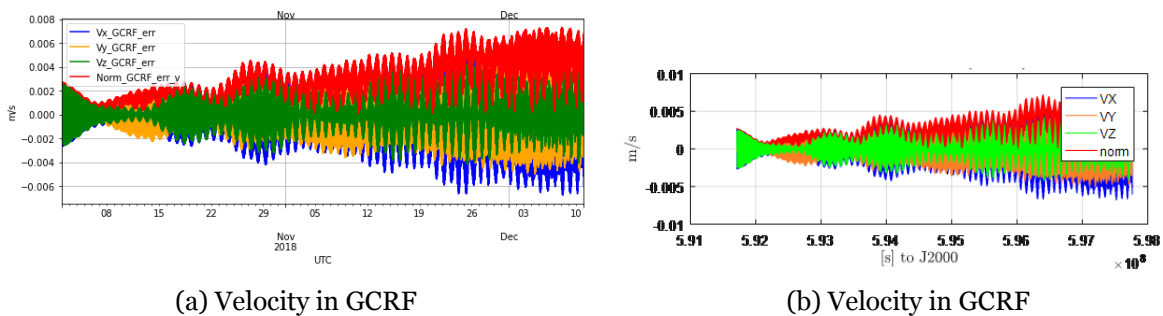(a) Velocity in GCRF

(b) Velocity in GCRF

Figure 3.4.2: EOP analysis - Navigator cross validation of IERS 2010 convention. Optimal scenario with unbiased EOPs

Fig. 3.4.4 shows a breakdown of position and velocity errors. Fig. 3.4.4a shows the position error. A time bias was added to the input of the simulator input. The time bias ranges from 1 ms to 10 days. The resulting position error ranges from 2 m up to 9×10^6 m for a 12h bias. Over the considered intervals, the polar motion contributes an order of magnitude less to the position and velocity errors. Fig. 3.4.4b shows the velocity error. The PV error is maximum for 12h. The error decreases significantly for a 1 day bias. For 12h bias, the ECEF frame is in the opposite direction so it was expected to have a maximum value. For one day bias the error is not zero (the value is close to 100km), probably due to the irregularity of UT1 causing an irregularity in Earth's rotation rate. Thus, the orientation of the ECEF frame after one day is not exactly the orientation of ECEF at t = 0. Table 3.4.3 shows similar errors as [8].

Bias EOP	Bias P	Bias V
TAI - UT1: 1 s	330 m	0,35 m/s
Polar motion: 1"	44 m	0,05 m/s

Figure 3.4.3: Estimation of error arising from EOP bias at 800 km altitude
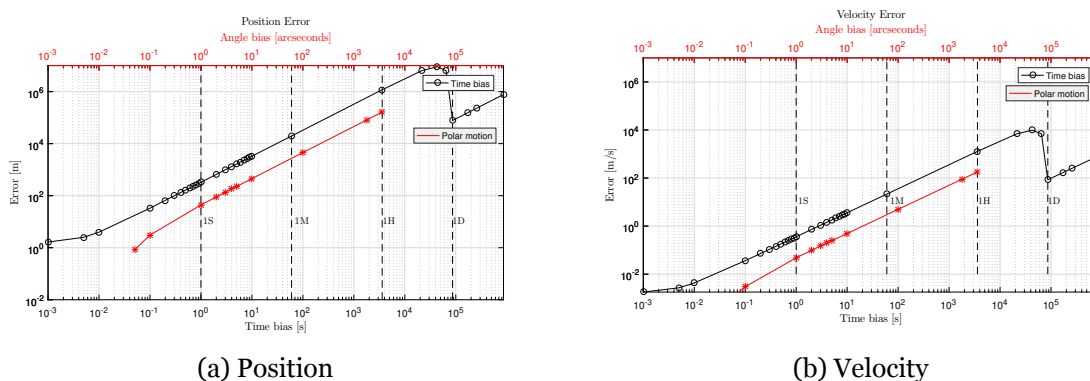

(a) Position

(b) Velocity

Figure 3.4.4: Effect of timing and polar motion on Position and Velocity frame conversion at altitude LEO 550 km.

With the tools developed for the navigation block, the error arising from the frame conversion was estimated. For a given precision requirements, the acceptable EOP error can be estimated. It allows to make a choice for the EOP estimation strategy and update rate.

Chapter 4

The IONOS simulator

The use of GNSS on board a satellite platform improves the availability of a navigation solution. However, the performance given in terms of PVT accuracy in Table 2.1.5 is based on several assumptions : clear sky visibility, quiet space weather conditions, no jamming and no multipath effect. Clear sky visibility is a valid assumption as long as the antenna is mounted on an unobstructed panel. Multipath on a satellite would also be very limited. The attitude dynamics of the satellite are also problematic. For example, the position of a tumbling spacecraft scenario is difficult to determine because the signal cannot be locked (as it happened with the JUICE spacecraft at the early stage during the Launch and Early Operations Phase (LEOP) phase). Other examples of interest are when the satellite is pointing at nadir or zenith, or when the attitude is controlled by a safe mode (with a particular direction to the sun). Those cases were investigated below.

GNSS constellations visibility and a Dilution of Precision analysis was conducted based on a simulated LEO orbit and a chosen attitude of the KINEIS spacecraft. To this end, an attitude control and orbit propagation library was developed. The main error sources affecting the GNSS measurements were included with the NTCM model. The simulator was validated against the navigation data of ANGELS satellite.

4.1   Goal

NMEA GSA sentences (see Method Section) from ANGELS GPS were provided. They were compared with the DOP statistics calculated by IONOS. Error sources (breakdown presented in the background section.) with simple statistics and simplifying assumptions to estimate the UERE were also computed by IONOS. DOP and UERE can be used to estimate the positioning error. The validation of individual models for each of the errors is beyond the scope of this work (see the following thesis for detailed explanation about ionospheric activity and multipath

modelling [32]). Therefore, the work focused on the identification of existing models and the selection for implementation.

Errors were assumed to have a zero mean and similar variances. These assumptions are not always verified. The simulator aims to quantify the error sources. A validation process has to be implemented with real data from LEO missions and proven software such as gLAB. After the validation, IONOS was developed to understand the impact on the navigation solution accuracy in the case of a limited FOV and high ionospheric activity.
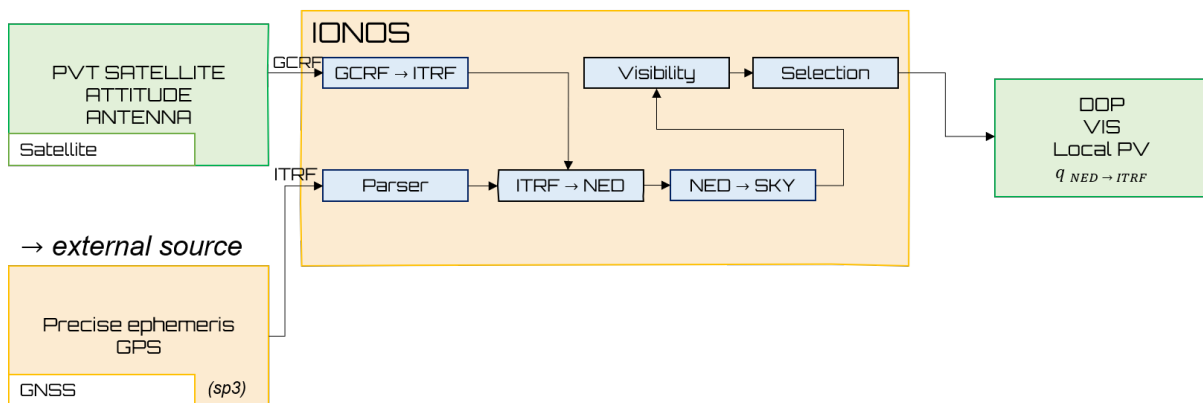
4.2   Features

Figure 4.2.1: General Architecture of IONOS

Fig. 4.2.1 shows the different features of IONOS. GNSS satellites coordinates were extracted from a precise ephemeris file, stored in sp3 format. A Matlab routine developed for the thesis. GNSS satellites coordinates are expressed in km in a ECEF frame . Lagrangian interpolation was used (see Methods section) for epochs between two entries of the sp3 ephemeris. Lagrangian polynomial interpolation of order 10 is recommended to ensure a cm level accuracy. Order 3 was used for the clock, as it shows a better stability. The orbit over a day was divided into small arcs of 10 sp3 epochs (i.e. 50 min for each arc). Each arc was interpolated at a sampling rate of 1 Hz. Fig. 4.2.2 shows the ITRF coordinates extracted from a sp3 file of the GPS satellite with PRN G01. Each sp3 file contains 86400 s (1 day) of data.

The spacecraft position was provided as an input in GCRF. The attitude of SAT with respect to GCRF was provided. IONOS synchronises the simulation data and the precise ephemeris data. It calculates GNSS visibility, Earth blockage, mask blockage, Dilution of precision. Satellites with highest elevation were selected. ITRF coordinates were retrieved using the NAV block described in the previous chapter. EOPs were estimated using the libraries described in the IERS section. The user position, known as the origo, is the centre of mass (CoM) of the LEO spacecraft. It is used by the ITRF $\longrightarrow$ NED function in IONOS. The CoM is given as an input of
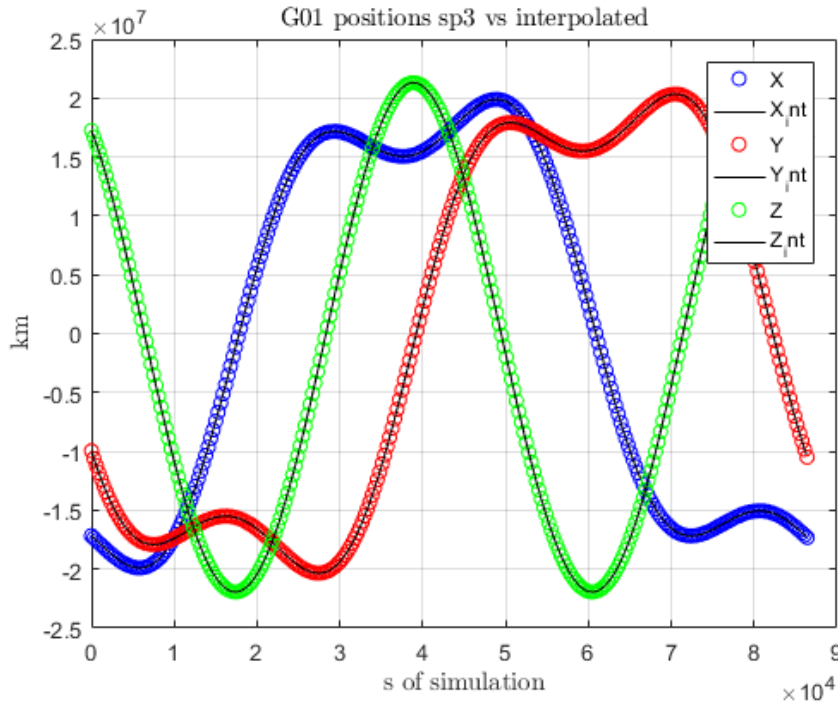
Figure 4.2.2: Precise ephemeris, 300s sampling (in colors), 1Hz interpolation (black solid line). Unit is meter.

the simulation. The orbit of the CoM was calculated with a reference propagator. However it was propagated in GCRF coordinates and ITRF $\longrightarrow$ NED requires ITRF coordinates, so the Navigator library (see IERS 2010 section) was used to convert inertial coordinates of the CoM to terrestrial coordinates. For each time step, the range between the user satellite and the constellations is calculated (GPS, GALILEO, BEIDOU, GLONASS, QZSS). The local NED (North, East, Down) frame is updated, the SAT frame is rotated according to the input quaternion. The ANT frame is fixed with respect to the satellite body. The frame rotations are summarised in Fig. 4.2.1.
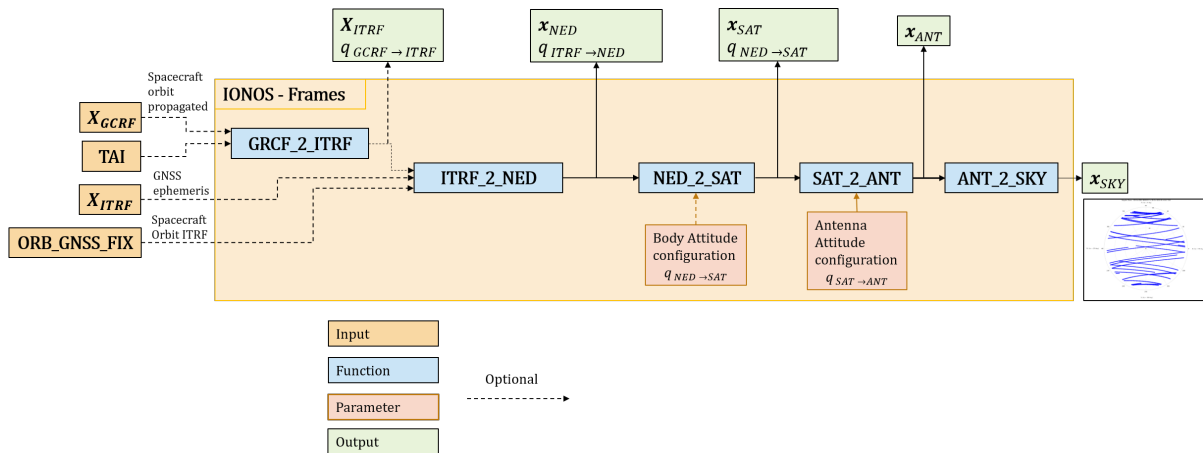

Figure 4.2.3: IONOS - Frames: Architecture of the frame conversion chain, from GCRF to local antenna frame.

Four rotations were calculated. They were expressed as quaternions (see Method Section). The first rotation requires the TAI time to convert a position vector expressed in GCRF coordinates to ITRF coordinates. This is done using the IERS 2010 convention (see IERS 2010 section). The current spacecraft position is given in ITRF and it is used as the input of the ITRF $\longrightarrow$ NED function. If the spacecraft orbit was propagated, the position should be converted to the ITRF frame. The ITRF coordinates were then converted to geodetic coordinates (latitude, longitude and height based on the reference WGS84 ellipsoid) (see Background section). The NED (North, East, Down) frame was defined with origin at the centre of mass of the spacecraft.

The spacecraft is not always aligned with the NED frame (it is rarely the case). The set of 3-2-1 Euler angles (h, b, φ) describes this frame rotation. The convention used is the following: angles were defined from the NED frame to the satellite body frame (SAT). Rotations were defined as *intrisic* rotations, i.e. about rotated axes. The DCM that converts a vector expressed in NED to SAT coordinates is given by :

$$[\mathbf{SN}] = [\mathbf{R_3}(h)][\mathbf{R_2}(b)][\mathbf{R_1}(\varphi)] \tag{4.1}$$

The corresponding quaternion is :

$$q_{\text{NED} \longrightarrow \text{SAT}} \tag{4.2}$$

Eventually, the orientation of the antenna was described with respect to the satellite body frame. Angles are defined from ANT frame to SAT frame. They were given as an input of SAT $\longrightarrow$ ANT function. The antenna was considered to be aligned with +Za. The DCM converting a vector expressed in SAT to ANT coordinates is given by :

$$[\mathbf{AS}] = [\mathbf{R_3}(-h)][\mathbf{R_2}(El)][\mathbf{R_1}(b)] \tag{4.3}$$

The corresponding quaternion is :

$$q_{\text{SAT} \longrightarrow \text{ANT}} \tag{4.4}$$

The following tables describe some default configurations of the satellite body frame and the antenna frame :

Table **??** shows sets of 3-2-1 Euler angle and the resulting alignment of NED and SAT frames. For example, when (h, b, φ) = (0,0,-90) deg, X_{SAT} is aligned with $\mathbf{e}_N$ direction, Y_{SAT} is aligned with $\mathbf{e}_D$, and X_{SAT} is aligned with $-\mathbf{e}_E$.

Table. shows sets of 3-2-1 Euler angle and the resulting alignment of ANT and SAT frames. For example, when (h, b, φ) = (0,0,-90) deg, X_{SAT} is aligned with $\mathbf{e}_N$ direction, Y_{SAT} is aligned with

Table 4.2.1: NED to SAT Euler angles and related configurations. h,b,φ represent a 3-2-1 rotation sequence about NED axes.

h	b	φ	$X_{\mathbf{SAT}}$	$Y_{\mathbf{SAT}}$	$Z_{\mathbf{SAT}}$
0	0	0	N	E	D
0	0	-90	N	D	-E
0	-90	0	-D	E	N
0	0	180	N	-E	-D

Table 4.2.2: Some angles and related configurations of Antenna frame (ANT) relative to satellite body frame (SAT).

-h	El	b	$X_{\mathbf{ANT}}$	$Y_{\mathbf{ANT}}$	$Z_{\mathbf{ANT}}$
0	0	0	X_{SAT}	Y_{SAT}	Z_{SAT}
0	0	90	X_{SAT}	Z_{SAT}	$-Y_{\text{SAT}}$
0	0	180	X_{SAT}	$-Y_{\text{SAT}}$	$-Z_{\text{SAT}}$

$\mathbf{e}_D$, and X_{SAT} is aligned with $-\mathbf{e}_E$.

There are two additional parameters : the lever arm describes the offset between the satellite centre of mass and the antenna. The second parameter is the Antenna Phase centre offset, it describes the point at which the pseudorange measurement is performed. These two parameters were set to zero in the simulations.

Eventually, GNSS satellites positions were computed in the local antenna frame in terms of Azimuth, elevation and slant distance. Positive elevations were counted along - Za, and negative elevations were counted along +Za (i.e. in the antenna hemisphere).

The simulation configuration parameters were defined in a Matlab structure IONOS.

```matlab
IONOS.PARAM_ORB_SRC = 'REF'; % 'kineis'      % orbit source
IONOS.PARAM_ORB = 'LEO';         % 'MEO' % 'GEO' % orbit type
IONOS.PARAM_INC = 'Equatorial';  % 'Polar'      % inclination


IONOS.PARAM_sp3_parsing = 1;          % parsing sp3 to matlab
IONOS.PARAM_interpolation = 0;        % sp3 interpolation
IONOS.PARAM_constellation_orbit = 1; % plot GNSS constellation



IONOS.PARAM_GPS = 1;     % plotting GPS ; DOP computation with GPS
IONOS.PARAM_GALILEO = 1; % plotting GALILEO
```

```
IONOS.PARAM_GLONASS = 0; % plotting GLONASS
IONOS.PARAM_BEIDOU = 0;  % plotting BEIDOU
IONOS.PARAM_QZSS = 0;    % plotting QZSS


IONOS.PARAM_REF_DATUM = 'WGS84'; % 'GRS80' % Geoid reference
IONOS.PARAM_ANT_CONF = 'Default'; % 'Obstacle'
IONOS.PARAM_SAT_ATT = 'NED'; % Attitude of SAT wrt NED frame.
% for 'NED', X_sat = N, Y_sat = E, Z_sat = D =
IONOS.PARAM_ANT_ATT = 'XZ-Y'; % Attitude of SAT wrt NED frame.
% for 'XZ-Y', X_ant = X_sat, Y_ant = Z_sat, Z_ant = -Z_sat


IONOS.PARAM_ID_TEST = 'G01';  % GPS GNSS satellite G01
```

The orbit type and inclination parameters enable to select the correct input file. For example, choosing IONOS.PARAM_ORB_SRC = 'REF', IONOS.PARAM_ORB = 'LEO' and IONOS.PARAM_INC = 'Equatorial' will result in a LEO equatorial orbit for the CoM, propagated with a reference orbit propagator. The parsing from the standard sp3 file format to a Matlab double matrix can be turned on or off. Lagrange interpolation can also be turned on or off. Constellations can be selected for plotting. DOP was computed for the GPS constellation only. The antenna can be configured with Default mode (no elevation mask, 180 °FOV) or in Obstacle mode (tunable elevation mask). The following table summarizes several default configurations :

Earth blockage was accounted in IONOS. Given an ellipsoid of semi-major axis a along x and y axis, and b along z axis, the intersection of an ellipsoid and a line defined by a point and a unit vector (A,$\vec{u}$), yields the following equation. Solving this equation for t allows to determine a condition for a satellite visibility.

$$\frac{(x_A + t \cdot u_x)^2}{a^2} + \frac{(y_A + t \cdot u_y)^2}{a^2} + \frac{(z_A + t \cdot u_z)^2}{b^2} = 1 \qquad (4.5)$$

Fig. 4.2.4 shows the spacecraft in a LEO orbit as seen from the north celestial pole. The antenna is pointing towards the upper part of the figure. Satellites on the left part are visible, satellites on the right are blocked by the Earth.

The simulator determines the visibility of GNSS constellations. GNSS constellations visibility and DOP variation vs number of visible satellites was assessed. Theoretical considerations regarding DOP can be found in [39], [5]. According to [39], the lowest GDOP achievable is 1.581 with a negative elevation of 19.47°.
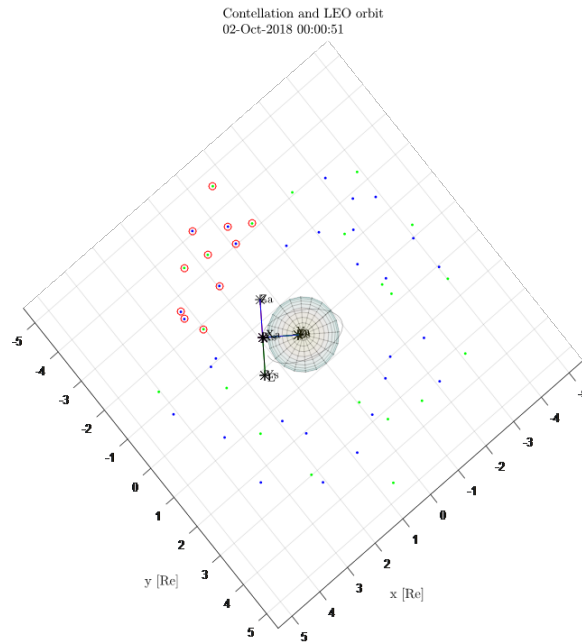
Figure 4.2.4: Earth visibility blockage

Thus, a negative correlation should be observed for DOP and the number of visible satellites, with high increases of DOP when the number of satellites is low. A short description of inputs, outputs and test cases for unit functions of the code is provided in the Annex section.Unit tests were conducted to validate the implementation of DOP and GNSS constellations visibility analysis functions.

4.3 Functional validation

The next section validates the function in charge of computing DOP.

4.3.1 DOP unit testing

The origin of the local frame was centered on the spacecraft center of mass. Without loss of generality, one satellite was supposed to be at zenith, at a unit distance of the spacecraft.

The selected test cases are the following :

1. 1 satellite at zenith and 3 satellites equally spaced in azimuth every 120 °. All satellites have the same elevation. Elevations from -90 °to +90 °with step 5 °were tested.

2. 1 satellite at zenith and 5 satellites equally spaced in azimuth every 72°. All satellites have the same elevation. Elevations from -90 °to +90 °with step 5 °were tested.
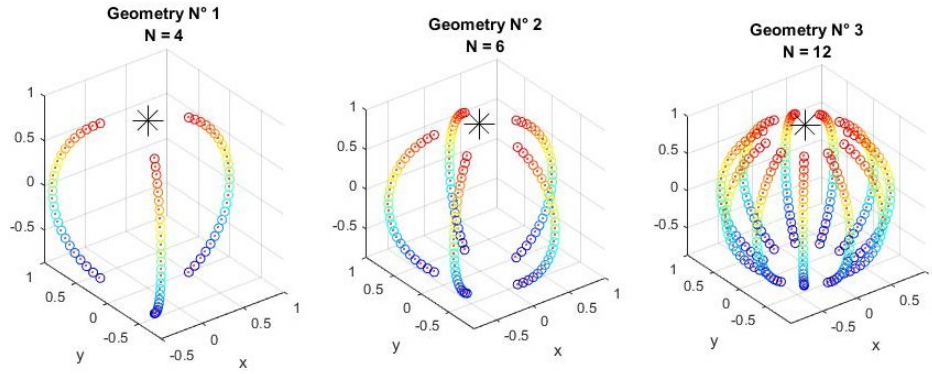
Figure 4.3.1: Satellite constellation geometry with 4,6,12 visible satellites

3. 1 satellite at zenith and 11 satellites equally spaced in azimuth every 32.7 °. All satellites have the same elevation. Elevations from -90 °to +90 °with step 5 °were tested.

In the case of four visible satellites, the elevations are $(0, \theta, \theta, \theta)$ (with $\theta < 0$ on Fig. 4.3.10. The azimuth are (0,0,120°,240°). Using the conversion from cartesian to spherical coordinates, satellites have the coordinates :

$$
\begin{aligned}
\mathbf{x}_1 &= (\quad 0, \quad\quad 0, \quad\quad 1 \quad) \\
\mathbf{x}_2 &= (\quad \cos\theta, \quad\quad 0, \quad\quad \sin\theta \quad) \\
\mathbf{x}_3 &= (\quad -\cos\theta/2, \quad \sqrt{3}/2\cos\theta, \quad \sin\theta \quad) \\
\mathbf{x}_4 &= (\quad -\cos\theta/2, \quad -\sqrt{3}/2\cos\theta, \quad \sin\theta \quad)
\end{aligned}
\tag{4.6}
$$

The determinant of matrix $\mathbf{Q} = \mathbf{G}^{\mathrm{T}}\mathbf{G}$ is :

$$
\det(Q) = \begin{vmatrix} 3/2\cos\theta^2 & 0 & 0 & 0 \\ 0 & 3/2\cos\theta^2 & 0 & 0 \\ 0 & 0 & 3\sin\theta^2 + 1 & 3\sin\theta + 1 \\ 0 & 0 & 3\sin\theta + 1 & 4 \end{vmatrix} = \frac{27}{4}\cos\theta^4(\sin\theta - 1)^2 \tag{4.7}
$$

Thus, the determinant is zero (so the matrix is singular) for $\theta = \frac{\pi}{2} + k\pi, k \in \mathbb{Z}$. Using the formula :

$$
Q^{-1} = \frac{\operatorname{com}(Q)^{\mathrm{T}}}{\det(Q)} \forall \theta \neq \theta = \frac{\pi}{2} + k\pi, k \in \mathbb{Z} \tag{4.8}
$$

the inverse matrix wad derived and GDOP was derived :

$$\text{GDOP} = \text{Tr}(Q) = \frac{\sqrt{3\sin\theta^2 + 4\tan\theta^2 + 4\sec\theta^2 - 8\tan\theta\sec\theta + 5}}{\sqrt{3}|\sin\theta - 1|} \qquad (4.9)$$
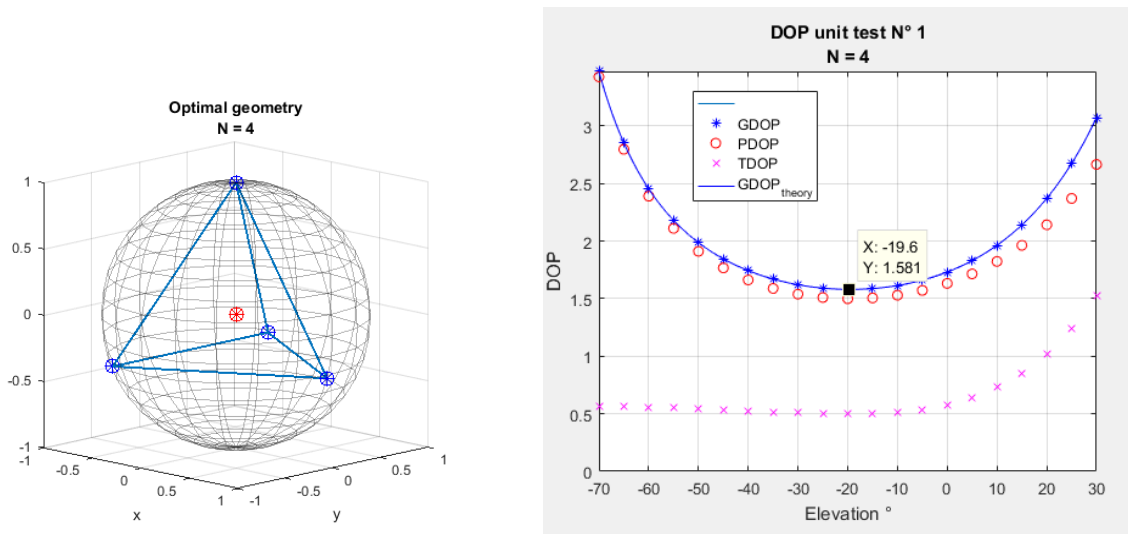

Figure 4.3.2: Left : Optimal constellation geometry with 4 satellites in view, Right: DOPs versus elevation with 120°spacing in azimuth. Theoretical GDOP computed with Eq. 4.9

The optimal geometry with four satellites was found to be three satellites with equal spacing at -19.47 °of elevation, with GDOP = $\sqrt{5/2} \simeq 1.5811$ and PDOP = 1.5. For 12 satellites in view, DOPs were smaller. Minimum GDOP was 1.1 and PDOP = 1.0.
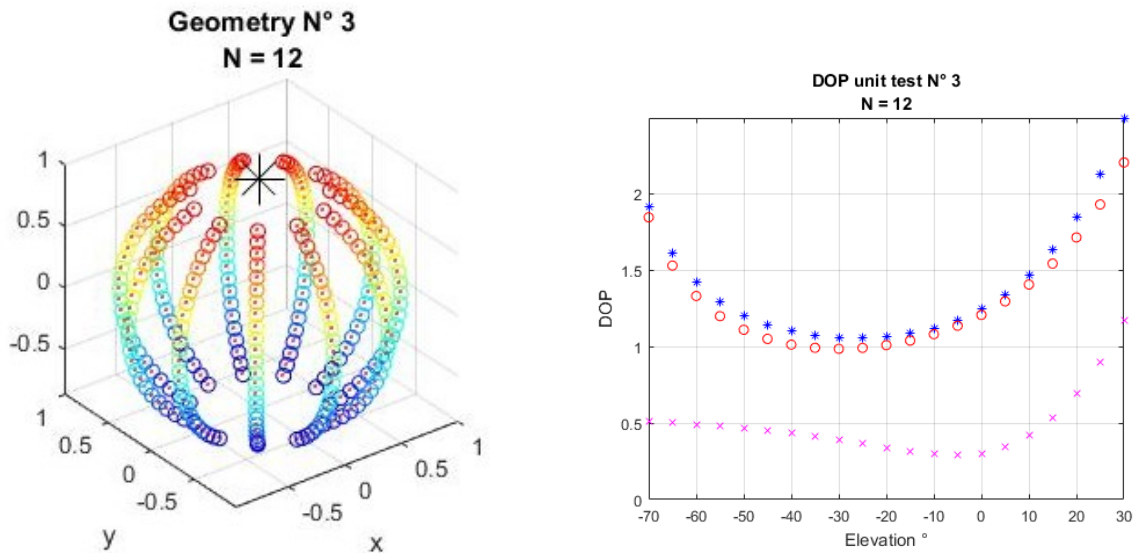

Figure 4.3.3: Left : Satellite Constellation geometry with 12 satellites in view, with 32.7 °space azimuth, Right : DOPs with 12 satellites in view (GDOP = blue stars; PDOP = red circles, TDOP = pink crosses
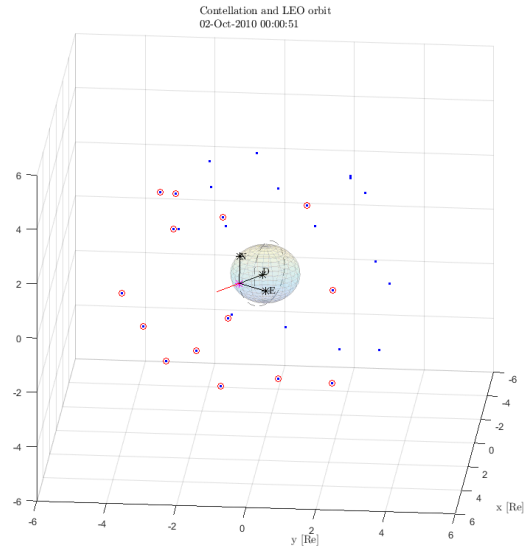
4.3.2 Orbit test cases

Several test case were identified with simple orbits and simple satellite geometry:

1. LEO equatorial orbit pointing zenith.

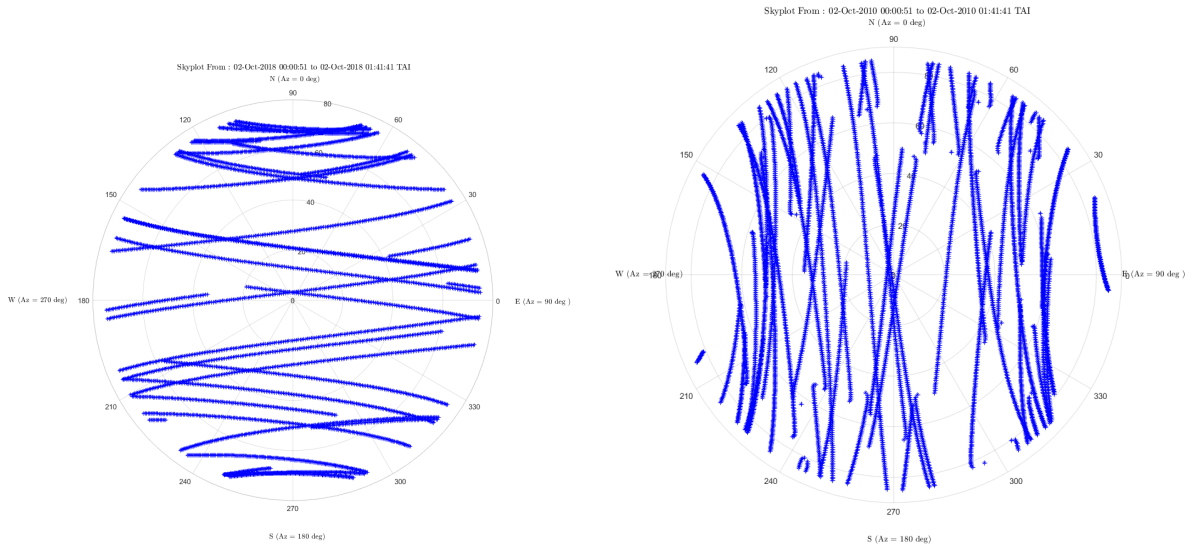2. LEO polar orbit pointing zenith.
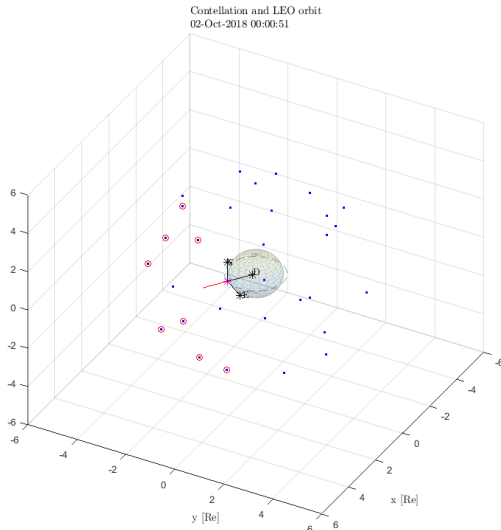
(a) LEO Equatorial, Zenith pointing

(b) LEO Polar, Zenith pointing

Figure 4.3.4: Orbit and constellations geometry
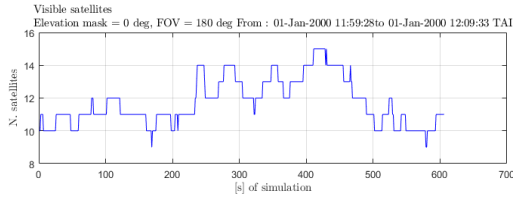

(a) LEO Equatorial, Zenith pointing

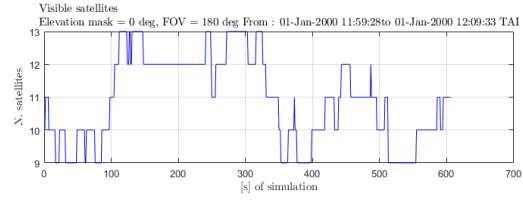
(b) LEO Polar, Zenith pointing

Figure 4.3.5: Skyplot of test cases.

Table 4.3.1 summarizes the GDOP statistics of the test cases:

The test case scenario are equatorial and polar LEO orbit where the satellite is always pointing nadir. Thus, the set of parameters (h, b, φ) from NED to SAT is 0. The angular velocity of the

65

(a) LEO Equatorial, Zenith pointing

(b) LEO Polar, Zenith pointing

Figure 4.3.6: GPS visibility for various test cases
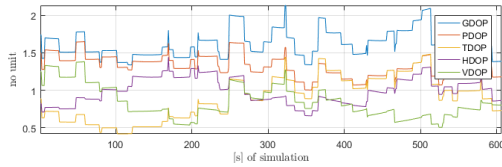
(a) LEO Equatorial, Zenith pointing
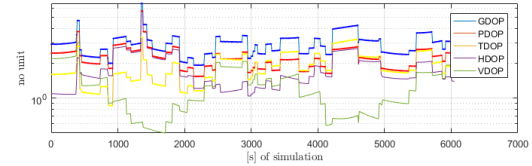
(b) LEO Polar, Zenith pointing

Figure 4.3.7: GPS DOPs for various test cases
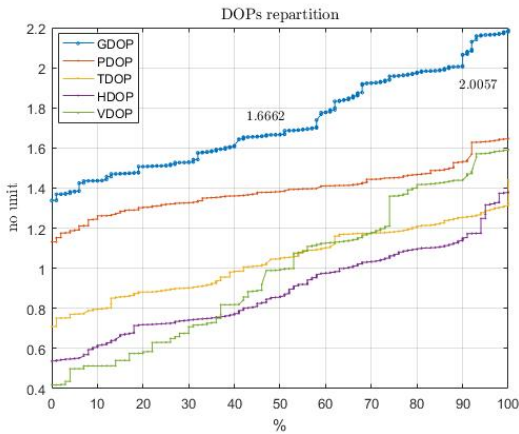
(a) LEO Equatorial, Zenith pointing
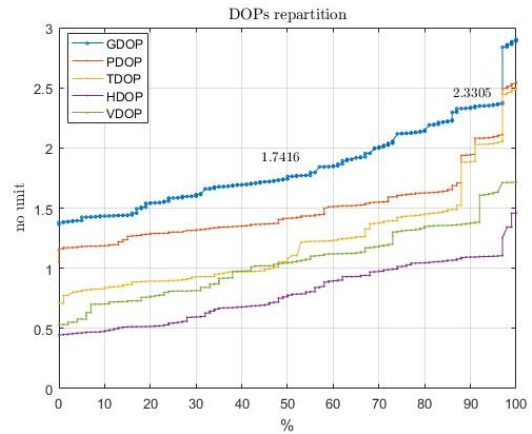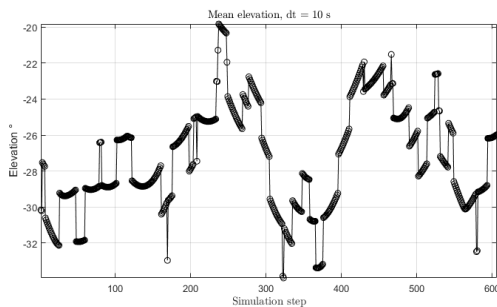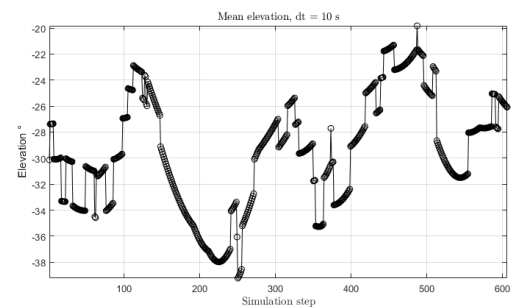
(b) LEO Polar, Zenith pointing

Figure 4.3.8: DOP repartition. 50 % and 90 % threshold represented

(a) LEO Equatorial, Zenith pointing

(b) LEO Polar, Zenith pointing

satellite with respect to the GCRF frame. The orbital period and the angular rate amplitude are defined as :

$$
\begin{aligned}
T &= 2\pi\sqrt{a^3/\mu_\oplus} \\
\omega &= 2\pi/T
\end{aligned}
\tag{4.10}
$$

66

Table 4.3.1: GDOPs statistics for LEO Equatorial and Polar orbits, zenith pointing. GPS satellites only. Last row shows results with highest elevation satellites and maximum 12 satellites.

Case	$\langle$GDOP$\rangle$	σ_{GDOP}	RMS	Min	Max
LEO Equ.	1.6157	0.1762	1.6252	1.3371	2.1300
LEO Pol.	1.778	0.3071	1.8041	1.2733	2.3959
LEO Pol. (selection)	1.839	0.3435	1.8709	1.3627	2.9015

Table 4.3.2: DOPs comparison. Selection indicates a maximum of 12 satellites, filtered by highest elevation

Case	$\langle$GDOP$\rangle$	$\langle$PDOP$\rangle$	$\langle$HDOP$\rangle$	$\langle$VDOP$\rangle$	$\langle$TDOP$\rangle$
LEO Equ. (Selection)	1.73	1.39	1.04	0.89	0.98
LEO Pol. (selection)	1.84	1.49	1.21	0.79	1.05

Given $R_{\oplus} = 6.378 \times 10^6$ m, $\mu_{\oplus} = 3.986 \times 10^{14}$ m³/s²,

- LEO equatorial : z = 450 km, T = 5615 s, $\omega = 1.12 \times 10^{-3}$ rad/s $\mathbf{e}_N$

- MEO equatorial : z = 20 000 km, T = 39 600 s, $\omega = \pm 1.5 \times 10^{-4}$ rad/s $\mathbf{e}_N$

- GEO equatorial : z = 36 000 km, T = 86 400 s, $\omega = 7.3 \times 10^{-5}$ rad/s $\mathbf{e}_N$

(a) LEO 450 km   (b) MEO 20 000 km   (c) GEO 36 000 km
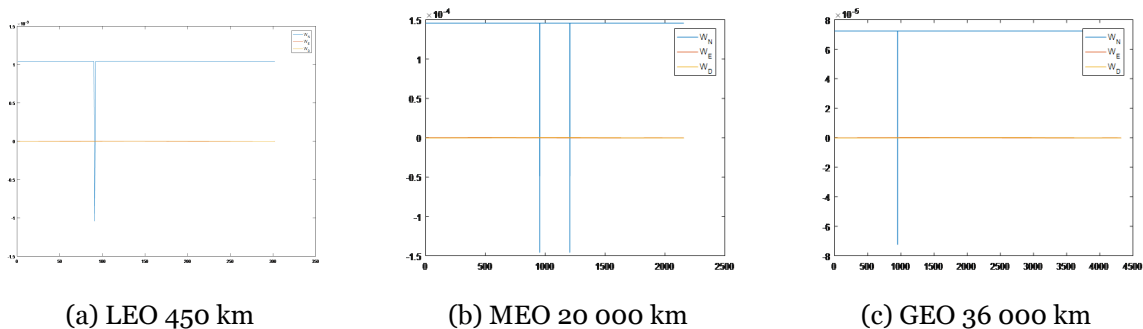
Figure 4.3.10: Angular velocity of NED frame with respect to GCRF. Angular velocity resolved in NED coordinates. All equatorial with nadir pointing. y unit is rad/s. x unit is simulation steps.

Fig. 4.3.10 shows that the angular rate is correctly computed, excepted for one or two epochs.

The rationale might be the crossing of a pole, which results in a u-turn of the NED frame.

4.4 ANGELS Flight data

PVT, GPS visibility and DOP data from ANGELS were provided by HEMERIA. The results are shown in Fig. 4.4.3. Data were provided every 16 seconds, (0.0625 Hz), starting 2022/06/15 00:00:13 UTC. Data extends to 2022/06/24 23:59:45 UTC. Elevation mask was set to 0°.

(a) Positions   (b) Velocities   (c) DOP and visibility
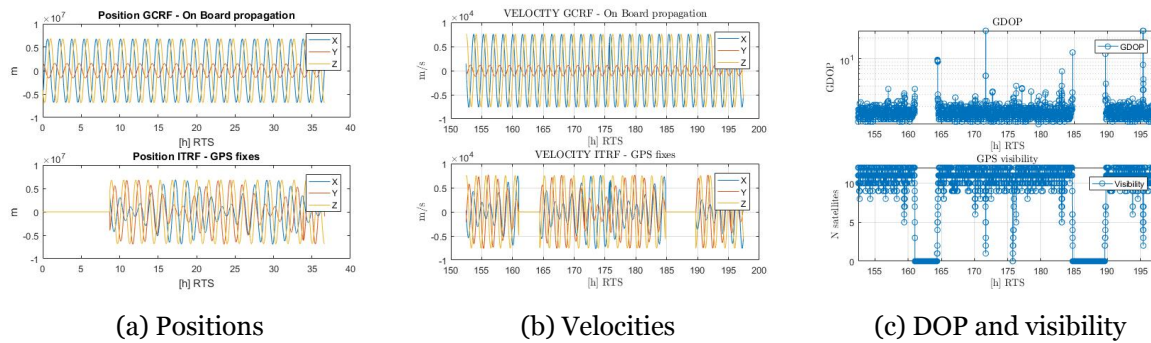
Figure 4.4.1: ANGELS Input data

Fig. 4.4.3a shows the propagated position in inertial coordinates (in GCRF frame), from the on-board propagator (top). The GPS position fixes are shown in terrestrial coordinates (bottom). During the first 8 hours, no position could be obtained from the GPS. Fig. 4.4.3b shows the propagated velocities in inertial coordinates (in GCRF frame), from the onboard propagator (top). The GPS velocity fixes are shown in terrestrial coordinates (bottom). In ANGELS data, some periods show no GDOP and zero visible satellites. At hour 161 to hour 164 of flight data, the GPS could not provide PV solution (same for hour 185 to 190). Fig. 4.4.3c shows the GDOP value (top) and the number of visible GPS satellites (bottom). GDOP is zero when no PV solution is provided. The on board propagator and the GPS do not give the same information, because the reference frame is not the same. At the beginning this is due to the time required to search GNSS signals and lock the signal. There are other periods with no visibility and high DOP, which might be caused by jamming or system outage. The flight data extends upon 86400s, so GPS data was truncated at 86400 s as well. Also, the sampling rate in ANGELS data was not constant. Sampling periods of 1 to 17s, 24s, 25s and 26s were found. Therefore the data set was resampled at 1Hz with linear interpolation using the Matlab resample method. The period simulated with IONOS was 15-Jun-2022 10:34:37 UTC to 15-Jun-2022 15:01:17 (indices 3000 to 4000). The period was chosen to ensure there were no missing data. The flight data had a sampling rate of 1s after linear interpolation.

Fig. 4.4.2 shows a comparison of ANGELS data in DOP and GPS visibility. A threshold of 12 channels was implemented in the receiver parameters (IONOS.RX field). The satellites were sorted by elevation in the local frame. The rationale was that the GPS antenna usually has the highest gain near zenith, so the signal strength is likely to be maximum near the zenith.
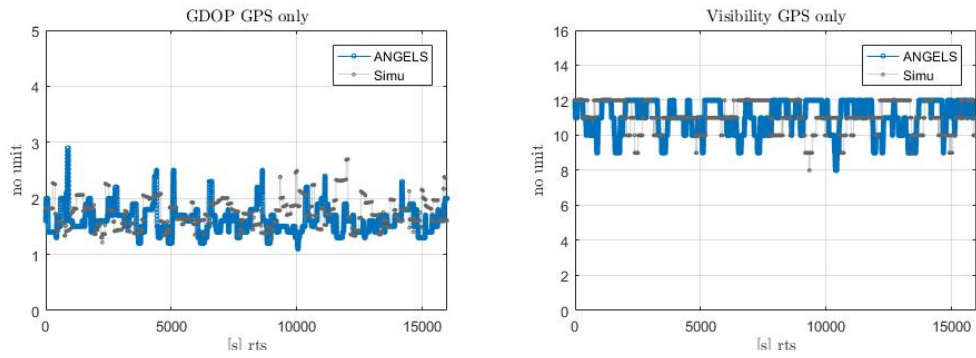
Figure 4.4.2: IONOS versus ANGELS (Zenith pointing)

(a) DOPs   (b) Visibility, DOPs, Attitude   (c) Visibility
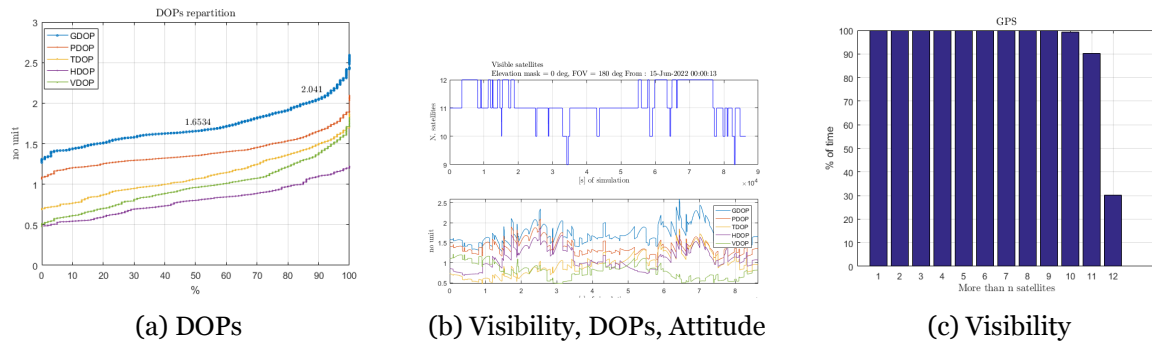
Figure 4.4.3: ANGELS simulation data over a day

Table 4.4.1: GDOPs statistics from IONOS simulation (NOM and SAM) and Flight Data for ANGELS, zenith pointing. GPS satellites only. Last row shows results with highest elevation satellites and maximum 12 satellites. Sample period is 15-Jun-2022 10:34:37 UTC to 15-Jun-2022 15:01:17

Case	$\langle$GDOP$\rangle$	σ_{GDOP}	50%	90%	Min	Max
ANGELS NOM	1.74	0.26	1.71	2.06	1.21	2.70
ANGELS NOM Flight Data / 10	1.61	0.24	1.6	1.9	1.1	2.9
ANGELS SAM	4.1	3.14	4.2	7.15	1.3	23.5
ANGELS SAM Flight Data / 10	4.7	5.51	2.8	9.5	1.3	25.5

The effect of a variable elevation mask on visibility and DOP were investigated. An elevation mask of 15 °was chosen, for all azimuth. For 0°elevation, mean GDOP is 1.74. With 15 °elevation, this number rises to 2.94. The average number of satellites dropped to 8. It suggests no elevation mask was present for ANGELS. This result is consistent with the fact that the antenna of ANGELS is free of obstacles on the satellite panel.

The spinning rate was set to 1 deg/s around Y_{SAT} axis. It is expected that the field of view is obstructed every 360 s because the satellite is pointing towards the Earth. Fig. 4.4.4 shows a periodic loss of visibility.

69

Table 4.4.2: Visibility statistics from IONOS simulation (NOM and SAM) and Flight Data for ANGELS, zenith pointing. GPS satellites only. First and third row shows results with highest elevation satellites and maximum 12 satellites. Sample period is 15-Jun-2022 10:34:37 UTC to 15-Jun-2022 15:01:17

Case	$\langle$ NSAT $\rangle$	σ NSAT	50%	90%	Min	Max
ANGELS NOM	11.2	0.77	11	12	8	12
ANGELS NOM Flight Data	11.1	0.95	11	12	8	12
ANGELS SAM	5.9	3.2	6	10	0	12
ANGELS SAM Flight Data	7.0	2.6	7	11	0	12
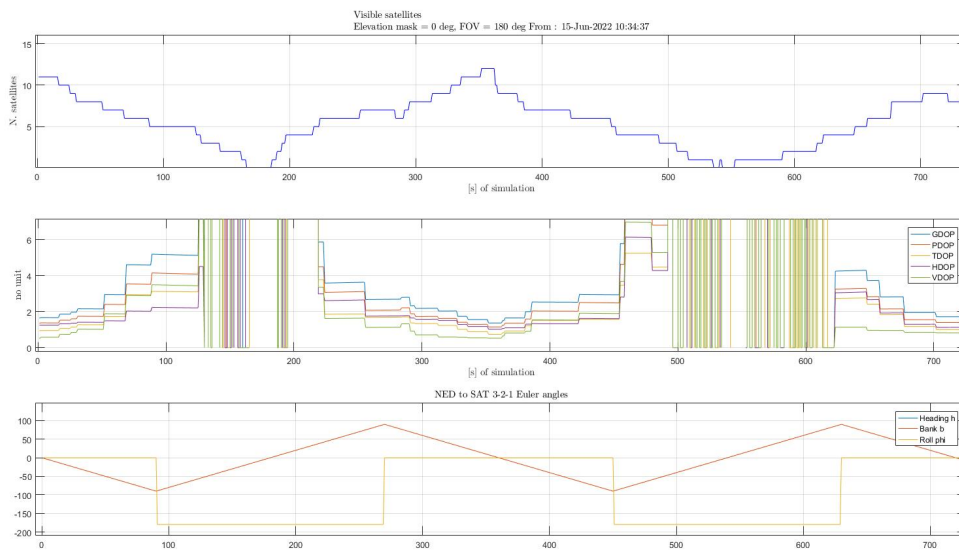
Figure 4.4.4: Simulated DOPs and visibility for ANGELS spinning

4.5   Discussion of results

Overall, the statistics of GDOP and satellite visibility were consistent between the simulation and flight data. The simulation reproduces faithfully the periodic loss of visibility and the periodic increase of GDOP (see Fig. 4.4.4 when the satellite is spinning). The average GDOP of the simulation data is higher than that of Flight Data (see Table 4.4.1). The average number of visible satellites between flight data and simulation was very similar. Overall, the average GDOP are similar to 8 %. The average GDOP of the simulation might be higher because of the elevation of the satellites in view. In both situation, a maximum of 12 satellites were used. Thus, the GDOP discrepancy cannot be explained with a higher amount of satellites observed for in the simulation.

A list of hypothesis was made to explain this discrepancy, sorted by order of confidence :

- The difference between number of visible satellites and number of satellites used to

compute a navigation fix is non negligible.

- Flight data, simulation data and GNSS precise ephemeris are not perfectly synchronised. The correlation of timeseries might exhibit a time delay.

- ANGELS receiver uses a different method to filter the satellites used to compute a navigation fix (e.g. filter with maximum signal power or no filter at all).

- An elevation mask prevents ANGELS from selecting satellites under a fixed elevation (e.g. 15 °)

The synchronisation may be detected by signal correlation. The statistics of the signals should be roughly the same. The GNSS receiver was placed on one of the panels on the platform, so the signals with low elevation should not be blocked in most of the cases. Also, the satellite might not be perfectly aligned with NED frame. The wobbling of the satellite might change the orientation of the antenna so that some satellites are out of view.

Since the antenna orientation can be changed at will, further analysis of the constellation visibility and GDOP can be conducted. Especially, the difference between antenna mounted on Y axis of the satellites and +Z axis can be anlaysed.

Chapter 5

Conclusions

The following questions were investigated throughout the thesis work :

- *How to implement the IERS 2010 convention with improved autonomy ?*

  The analysis of EOP and the selection of first order physical phenomena allowed to implement the IERS convention with a meter-level accuracy. With the onboard implementation of the convention, the PV information provided by the GNSS module is readily usable by onboard propagator.

- *Which error sources are dominant in the error budget in the context of a LEO spacecraft ?*

  The ionospheric delay was shown to be the main source of error uncorrected in the navigation solution of COTS receivers.

- *Which error sources removal methods are suited for real time corrections on board a LEO spacecraft with a single frequency GNSS receiver providing a navigation solution only ?*

  The Klobuchar model was not selected because it was not adapted for real time corrections in LEO orbit. The NTCM was used to provide TEC values. It was used for an external estimation of the navigation solution bias.

A COTS GNSS navigation system providing PVT information to the attitude control loop was investigated. The main difficulty of using COTS GNSS is that pseudoranges and carrier phase observations might not be available for real time navigation. Therefore, the work focused on developing real-time algorithms to convert the navigation PVT solution, given in a terrestrial frame. Using EOPs and a simplification of the IERS 2010 convention, an accuracy of 2 m and 1 mm/s was achieved for unbiased estimation of the EOPs. A non-optimal situation was also

investigated, suggesting a rapid growth of error in the case of poor time tagging or incorrect estimation of EOPs. Error sources were identified and suitable models for corrections were investigated. The NTCM model was found to be the most suited for real-time estimation of the ionospheric delay. The geometry matrix and dilution of precision calculated in the simulation showed good agreement with ANGELS flight data. The bibliography work exhibited a suitable model to estimate the ionospheric bias, scaled by the geometry matrix. This model could be implemented on-board. For a future work, using a single frequency GNSS receiver with access to the direct measurements of pseudoranges and carrier phase allows to calculate the GRAPHIC combination. This strategy allows to remove the ionospheric error so the external correction is no longer required. However, a strategy to solve the integer ambiguity of carrier phase measurements should be investigated. Using a Kalman filter with the combinations of each channel as states should be investigated further to improve the navigation solution.

Bibliography

[1] A. Scholz, F. König S. Fröhlich J. Piepenbrock. "Flight Results of the COMPASS-1 Mission". In: *Acta Astronautica, Volume 67, Issues 9-10* (2010).

[2] *An Overview of GPS receivers for small satellites.* URL: `https://blog.satsearch.co/2019-11-12-an-overview-of-gps-receivers-for-small-satellites`.

[3] Ashby, N. "Relativity in the Global Positioning System". In: *LivingReviews* (2003). URL: `https://www.livingreviews.org/Articles/Volume6/2003-1ashby`.

[4] Benoit, M. Casasco B. Girouart A. "GNC and AOCS functional chains engineering and verification". In: *8th ESA Workshop on Avionics, Data, Control and Software Systems - ADCSS 2014* (28 October 2014).

[5] Betz, J.W. *Engineering Satellite-Based Navigation and Timing.* John Wiley Sons, Inc., Hoboken, New Jersey, 2016.

[6] Blewitt. "Basics of the GPS Technique Observation Equations". In: *Geodetic Applications of GPS* (1997).

[7] Boschetti, I. Vanschoenbeek B. Bonhoure M. and Legenne, J. "GNSS Time Offset - Effects on GPS -Galileo Interoperability Performance". In: *Inside GNSS* (2007).

[8] Bradley, Ben K. "Influence of ITRS/GCRS Implementation for Astrodynamics: Coordinate Transformations". In: *Advances In Space Research* (2015).

[9] Bradley, Ben K. "Numerical Algorithms For Precise And Efficient Orbit Propagation". In: *University of Colorado at Boulder* (2015).

[10] Brouwer. "Solution of the problem of artificial satellite theory without drag, " in: *The Astronomical Journal* (1959).

[11] CNES. *Techniques et Technologies des Véhicules Spatiaux, Volume 3 : Plateformes.*

[12] *COMPASS-1 mission.* URL: `https://www.eoportal.org/satellite-missions/compass-1#orbit`.

[13] Coppola. "The IAU 2000 and IAU 2006 Precession nutation theories and their implementation". In: *Advances in the Astronautical Sciences* (2009).

[14] Correction, European GNSS (Galileo) Open Service Ionospheric. *Ionospheric correction algorithm for Galileo single frequency user*. 2016.

[15] Delacroix, L. Javanaud E. Dequeker S. Salas H. Darnès L. Gillot F. Viaud. N. Rey T. Cussac P. Larivière C. Rossiquet D. "ANGELS SmallSat Demonstrator for new French product line". In: *Space Ops Conference* (2018).

[16] Diggelen, Frank Van. *GPS/GNSS accuracy, Lies damn lies and statistics*. URL: `https://www.gpsworld.com/gpsgnss-accuracy-lies-damn-lies-and-statistics-1134/`.

[17] DLR. *Phoenix Spaceborne GPS Receiver*. Online Resource. 2007.

[18] Fälthammar, C-G. *Space Physics*.

[19] Ferrage, F.G. Lemoine N.P. Zelensky A. Belli A. Couhert G. Moreaux J. Saunier P. "The Synergy of Satellite Laser Ranging (SLR) and DORIS as Space Geodesy Techniques". In: *21st International Workshop on Laser Ranging* (2018).

[20] G. Xu, D. Chen X. Zhang W Liao. "Improvement of Orbit Prediction Algorithm for SpacecraftThrough Simplified Precession-Nutation Model UsingCubic Spline Interpolation Method". In: *Computer Modeling in Engineering Sciences* (2020).

[21] Gaylor. *Integrated GPS/INS Navigation System Design for Autonomous Spacecraft Rendez-vous*. 2003.

[22] Georgy, Aboelmagd Noureldin Tashfeen B. Karamat Jacques. *Fundamentals of Inertial navigation, Satellite-based Positioning and their Integration*. Springer, 2013.

[23] Gill, EKA and Montenbruck, O. *Satellite orbits: Models, methods and applications*. English. Springer Science+Business Media, 2013. ISBN: 978-3-540-67280-7. DOI: `10.1007/978-3-642-58351-3`.

[24] GomSpace. *NanoSense GPS Kits Datasheet*. Online Resource. 2019.

[25] Group, Hemeria. *Hemeria group - About*. URL: `https://www.hemeria-group.com/a-propos/`. Visited on 23/02/2023.

[26] *GSSC Now Portal*. URL: `https://gssc.esa.int/portal/?vuePage=1&size=20&mode=query&sortOption=recent&query=RINEX4`.

[27] H., Hofmann-Wellenhof B. Lichtenegger and E., Wasle. *GNSS Global Navigation Satellite Systems*. 2008.

[28] Hećimivić, Ž. "Relativistic effects on satellite navigation". In: *Tehnicki Vjesnik* (2013).

[29] Hernandez-Pajares, J. Sanz Subirana J.M. Juan Zornoza M. *GNSS Data Processing, Vol. I: Fundamentals and Algorithms*. ESA Communications, 2013.

[30] Hilton. "Report of the international astronomical union division Working group on precession and the ecliptic". In: *Celestial Mechanics and Dynamical Astronomy* (2006).

[31] J.L. Gerner J.L. Issler D. Laurichesse C. Mehlen N. Wilhelm. *TOPSTAR 3000 − An Enhanced GPS Receiver for Space Applications*. ESA Bulletin. 2000.

[32] Jakobsen. "Ionospheric variations and characteristics of multipath". In: ().

[33] JJ. Miller, J. Parker. "NASA GNSS Activities - WG-B 6Enhancement of GNSS Performance, New Services & Capabilities". In: International Committee on Global Navigation Satellite Systems (ICG) Working Group, 2017.

[34] Johnson, S. Malys R. Solomon J. Drotar T. Kawakami T. "Compatibility of Terrestrial Reference Frames used in GNSS broadcast messages during an 8 week period of 2019". In: *Advances in Space Research* 67.2 (2021), pp. 834–844. DOI: `https://doi.org/10.1016/j.asr.2020.11.029`.

[35] Kelso, Dr. T.S. *NORAD GP Element Sets Current Data Current as of 2023 Jul 02 14:05:30 UTC (Day 183)*. URL: `https://celestrak.org/NORAD/elements/gp.php?GROUP=gps-ops&FORMAT=json`.

[36] Kelso, Dr. T.S. *NORAD GP Element Sets Current Data Current as of 2023 Jul 02 14:05:30 UTC (Day 183)*. URL: `https://celestrak.org/NORAD/elements/gp.php?GROUP=galileo&FORMAT=json`.

[37] Krynski, Jan. "Major concepts of recent celestial and terrestrial reference systems". In: *Annual of Navigation* 8 (Jan. 2004), pp. 5–20.

[38] Kwon, Ghangho Kim Sanghoon Jeon Changdon Kee Tae Soo No Kiho and Choi, Seungwoon. "Gps Satellite State Vector Determination In ECI Coordinate System Using The Civil Navigation Message". In: *The journal of Navigation* (2014).

[39] Langley, Richard B. "Dilution of Precision". In: *GPS World* (1999).

[40] Leppinen. "Integration of a GPS subsystem into the Aalto 1 nanosatellite". Master Thesis. Department of Automation and System Technology, Aalto university, 2013.

[41] Markgraf Montenbruck, Hauschild. "GPS Receiver Performance On Board a LEO Satellite". In: *InsideGNSS* (2014).

[42] Montenbruck, M. Garcia Fernandez O. "Low Earth orbit satellite navigation errors and vertical total electron content". In: *Radio Science* (2006). DOI: `10 . 1029 \ /2005RS003420`.

[43] Montenbruck O., Gill E. *Satellite Orbits*.

[44] NASA. *NASA Technology Taxonomy*. Online Resource. 2020.

[45] NASA. *SOA 2022 − Guidance, Navigation, and Control*. URL: `https://www.nasa.gov/smallsat-institute/sst-soa/guidance-navigation-and-control`.

[46] NASA. *SOFA TimeScale and Calendar Tools*. Online Resource. 2010. URL: `http://www.iausofa.org/`.

[47] *Navigation Office ESA*. URL: `http://navigation-office.esa.int/products/gnss-products/`.

[48] Novatel. *OEM4-G2L Data Sheet V5A*. GPS World. 2006.

[49] Novatel. *OEMV-1 Data Sheet V5A*. Novatel. 2011.

[50] O, Montenbruck. "Precision real-time navigation of LEO-satellite using global positioning system measurements". In: *GPS Solution* (2008).

[51] O., Montenbruck. "GPS for Microsatellites - status and perspectives". In: *Small Satellites for Earth Observation* (2007).

[52] Observatoire de Paris, U.S. Naval Observatory. "Explanatory supplement to IERS bulletin A and bulletin BC04". In: (2014).

[53] Petit G., Luzum B. "IERS Convention (2010)". In: (2010).

[54] Poids et mesures de Paris, Observatoire des. *Rotation Matrices*. URL: `https://hpiers.obspm.fr/eop-pc/index.php?index=rotation&lang=en`.

[55] Poids et mesures de Paris, Observatoire des. *UT1*. URL: `https://hpiers.obspm.fr/eop-pc/index.php?index=UT1&lang=en#grav`.

[56] EO-portal. *(IZN-1) Laser Ranging Station in Tenerife, Spain, tracking satellites and debris*. URL: `https://www.eoportal.org/other-space-activities/izn-1-laser#esas-new-iza%5C%C3%5C%B1a-1-izn-1-laser-ranging-station-in-tenerife-spain-tracking-satellites-and-debris`.

[57] EO-portal. *DORIS Ground Tracking*. URL: `https://www.eoportal.org/satellite-missions/doris#ground-segment`.

[58] Ramos-Bosch, Pere. *Improvements in autonomous GPS navigation of Low Earth Orbit satellites*. Department of Applied Mathematics and Applied Physics UPC, Spain, 2008.

[59] *Running total*. URL: `https://www.nanosats.eu/`.

[60] S. Subirana. *Kinematic Orbit Estimation of a LEO satellite*. Online Resource.

[61] Satellite Surrey Technology. *Space GNSS Receiver SGR-Axio*. Online Resource. 2015.

[62] Satellite Surrey Technology. *Space GNSS Receiver SGR-Ligo*. Online Resource. 2015.

[63] Schaub, H. *Analytical Mechanics of Space Systems*. 2014.

[64] Serre, O. Montenbruck J-L. Issler F. Mercier S. Santandrea A Garcia J. Naudet S. "GPS-Based Precise Orbit Determination and Real-Time Navigation of the PROBA-2 Spacecraft". In: *5th ESA Workshop on Satellite Navigation User Equipment Technologies* (2010).

[65] SkyFox Labs. *Active GPS+GALILEO Patch Antenna piPATCH-L1E1 Product Datasheet*. Online Resource. 2020.

[66] *Smallsats and Cubesats GPS antennas and GNSS systems*. URL: `https://blog.satsearch.co/2021-02-16-smallsat-and-cubesat-gps-antennas-and-gnss-systems`.

[67] Surivet, A. "Integration and validation of a nanosatellite flight software (ESA OPS SAT project)". Master Thesis. Stockholm, Sweden: KTH Royal Institute of Technology, School of Engineering Sciences, 2021.

[68] Tilmans, O. Montenbruck P. Swatschina M. Markgraf S. Santandrea J. Naudet E. "Precision spacecraft navigation using a low cost GPS receiver". In: *GPS Solution* (2011).

[69] Trimble. *NMEA-0183 messages: Overview*. URL: `https://receiverhelp.trimble.com/alloy-gnss/en-us/NMEA-0183messages_MessageOverview.html`. Visited 21/03/2023.

[70] ublox. *u-blox M8 concurrent GNSS modules - Data sheet*. Online resources. 2022.

[71] Vallado, David A. "Using EOP and Space Weather Data for Satellite Operations". In: Presented as the 6th US Russian Space Surveillance Workshop, St Petersburg, Russia, 2005.

[72] Wallace, Capitaine. "Concise CIO based precession nutation formulations". In: *Astronomy and Astrophysics* (2008).

[73] Wallace, P. "Precession nutation procedures consistent with IAU 2006 resolutions". In: *Astronomy and Astrophysics* (2006).

[74] Weiß, Sascha. "Contributions to On Board Navigation on 1U CubeSats". Master Thesis. Berlin, Germany: TU Berlin, 2021.

[75] В. Г. Турышев. *Basics of Spacecraft Navigation*. Online Resource. 2011.

Appendix - Contents

Appendix A

First Appendix

A.1 Time formats

Time formats are a mean to specify an epoch. It can be a numeric count of days or seconds past some reference epoch (e.g. number of seconds past J2000 epoch). There are three widely used formats :

JD: The Julian Day is a continuous count of days and fractions thereof from the beginning of the year -4712. By tradition, the Julian Day begins at Greewich mean noon, that is, at 12h Universal Time.

MJD: The Modified Julian is also a continous count of days. It begins at Greenwich mean midnight.

Datetime : YYYY-MM-DD hh:mm:ss.sss or YYYY-MM-DDThh:mm:ss.sssZ

All epochs are provided with their time system (e.g. 59368 MJD TAI, 2456321 JD TAI, 2001-12-03 22:55:31 UTC). JD and MJD must *not* be used with UTC time scale because it is discontinuous. SOFA software implements the time system and formats conversions [46].

$$MJD = JD - 2400000.5 \tag{A.1}$$

A.2 Mathematical tools

Attitude parametrisation is discussed in the following. It is based on Schaub and Junkins [63] and Hoffmann-Wellenhof [27] reference books. It discusses the relevant mathematical concepts used in satellite navigation.

A.2.1 Direction Cosine matrix

The Direction Cosine Matrix (DCM) allows to transform a vector expressed in frame coordinate system A to a vector expressed in coordinate system B :

$$\mathbf{x}_B = [\mathbf{BA}] \, \mathbf{x}_A \tag{A.2}$$

The DCM rotating a frame about axis 1,2 and 3 respectively are given below :

$$
R_1(\alpha) = \begin{bmatrix} 1 & 0 & 0 \\ 0 & \cos(\alpha) & \sin(\alpha) \\ 0 & -\sin(\alpha) & \cos(\alpha) \end{bmatrix}
$$
$$
R_2(\alpha) = \begin{bmatrix} \cos(\alpha) & 0 & -\sin(\alpha) \\ 0 & 1 & 0 \\ \sin(\alpha) & 0 & \cos(\alpha) \end{bmatrix} \tag{A.3}
$$
$$
R_3(\alpha) = \begin{bmatrix} \cos(\alpha) & \sin(\alpha) & 0 \\ -\sin(\alpha) & \cos(\alpha) & 0 \\ 0 & 0 & 1 \end{bmatrix}
$$

A.2.2 Quaternions (Euler Parameters)

The quaternions require only four parameters to describe attitude instead of nine for DCM. The convention was scalar part as first parameters and vector part as parameters 2 to 4.

$$
\begin{aligned}
\beta_0 &= \cos(\Phi/2) \\
\beta_1 &= e_1 \sin(\Phi/2) \\
\beta_2 &= e_2 \sin(\Phi/2) \\
\beta_3 &= e_3 \sin(\Phi/2)
\end{aligned} \tag{A.4}
$$

where $\mathbf{e}$ is the principal rotation axis and Φ is the principal rotation angle. The DCM $[\mathbf{C}]$ associated to a quaternion is computed as:

$$
[\mathbf{C}] = \begin{bmatrix} \beta_0^2 + \beta_1^2 - \beta_2^2 - \beta_3^2 & 2\,(\beta_1\beta_2 + \beta_0\beta_3) & 2\,(\beta_1\beta_3 - \beta_0\beta_2) \\ 2\,(\beta_1\beta_2 - \beta_0\beta_3) & \beta_0^2 - \beta_1^2 + \beta_2^2 - \beta_3^2 & 2\,(\beta_2\beta_3 + \beta_0\beta_1) \\ 2\,(\beta_1\beta_3 + \beta_0\beta_2) & 2\,(\beta_2\beta_3 - \beta_0\beta_1) & \beta_0^2 - \beta_1^2 - \beta_2^2 + \beta_3^2 \end{bmatrix} \tag{A.5}
$$

The quaternion associated to a DCM $[\mathbf{C}]$ was computed using Markley's method. It ensures a

high numerical precision and the method is singularity-free.

A.2.3   Coordinates system tranformation

(a) NEU Frame

(b) Global ITRF to local NEU frame [27]

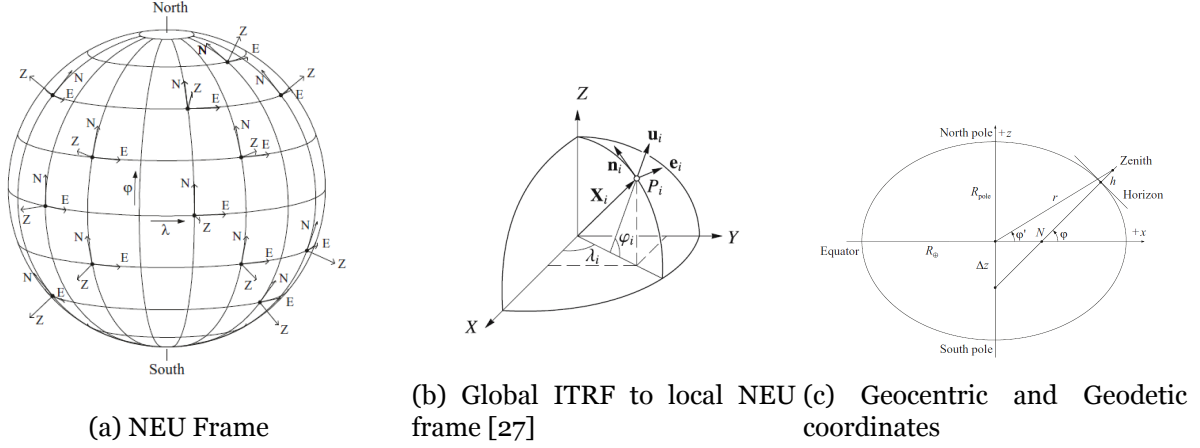(c) Geocentric and Geodetic coordinates

Figure A.2.1

The NEU frame is a local frame commonly used in navigation. The origin of the frame is the GNSS receiver. The unit frame vectors orientation depend on the center location, so that N points to the North, E to the East and U (or Z) to the zenith A.2.1a. The zenith direction used in GNSS measurements is defined by the normal vector to the ellipsoid. It differs from the local normal to the gravity potential lines. To convert from global terrestrial Cartesian coordinates (X, Y, Z) to global geodetic coordinates (latitude, longitude height), the following formula ([27]) yields a good approximation. Iterative methods and exact method (by Xu) can also be used. The approximate method was implemented :

$$
\begin{aligned}
\varphi &= \arctan \frac{Z + e^2 b \sin^3 \theta}{p - e^2 a \cos^3 \theta} \\
\lambda &= \arctan \frac{Y}{X} \qquad\qquad p = \sqrt{X^2 + Y^2} \\
h &= \frac{p}{\cos \varphi} - N \qquad\qquad \theta = \arctan \frac{Za}{pb} \\
e^2 &= \frac{a^2 - b^2}{a^2}
\end{aligned}
\tag{A.6}
$$

Then to convert from global to local Cartesian NEU coordinates, the transpose of the following matrix must be used :

$$
\mathbf{R}_i =
\begin{bmatrix}
- \sin \varphi_i \cos \lambda_i & - \sin \lambda_i & \cos \varphi_i \cos \lambda_i \\
- \sin \varphi_i \sin \lambda_i & \cos \lambda_i & \cos \varphi_i \sin \lambda_i \\
\cos \varphi_i & 0 & \sin \varphi_i
\end{bmatrix}
\tag{A.7}
$$

Eventually, the local Cartesian coordinates are related to the local spherical coordinates (geometric range s_{ij}, azimuth α_{ij} and zenith angle z_{ij}) :

$$
\mathbf{x}_{ij} = \begin{bmatrix} n_{ij} \\ e_{ij} \\ u_{ij} \end{bmatrix} = \begin{bmatrix} s_{ij} \sin z_{ij} \cos \alpha_{ij} \\ s_{ij} \sin z_{ij} \sin \alpha_{ij} \\ s_{ij} \cos z_{ij} \end{bmatrix} \tag{A.8}
$$

$$
\begin{aligned}
s_{ij} &= \sqrt{n_{ij}^2 + e_{ij}^2 + u_{ij}^2} \\
\tan \alpha_{ij} &= \frac{e_{ij}}{n_{ij}} \\
\cos z_{ij} &= \frac{u_{ij}}{\sqrt{n_{ij}^2 + e_{ij}^2 + u_{ij}^2}}
\end{aligned} \tag{A.9}
$$

A.2.4   Lagrangian interpolation

Given a set of $m + 1$ points $y(t_j)$, y quantity can be interpolated as following :

$$
\begin{aligned}
y(t) &= \sum_{j=0}^{m} L_j(t) \cdot y\left(t_j\right) \\
L_j(t) &= \prod_{k=0}^{m} \frac{t - t_k}{t_j - t_k}, \quad j \neq k
\end{aligned} \tag{A.10}
$$

$L_j(t)$ is a Lagrange polynomial, with $L_j(t_j)$ = 0. Lagrange polynoms of order 9 over data arcs of 10 points (duration of 50 min) were used to interpolate sp3 precise ephemeris at 1 Hz rate.

A.2.5   Error definitions

The rotational error is defined as the principal rotation angle between the reference frame and the frame resulting from the custom frame conversion implemented during the thesis work. Assuming the transformation matrix is $[\mathbf{T}]$ and the reference is $[\mathbf{T}_{\text{ref}}]$, the rotational error is Φ :

$$
\Phi = \text{DCM to Principal Rotation}([\mathbf{T}_{\text{ref}}] \, [\mathbf{T}]^{-1}) \tag{A.11}
$$

Then the geometric error at altitude z was defined as :

$$
\begin{aligned}
\mathrm{d}\mathbf{x} \quad &= \quad \mathbf{x}' - \mathbf{x}'_{\text{ref}} \quad = \quad [\mathbf{T}]\,\mathbf{x} - [\mathbf{T}_{\text{ref}}]\,\mathbf{x} \quad = \quad ([\mathbf{T}] - [\mathbf{T}_{\text{ref}}])\,\mathbf{x} \\
\text{with} \quad \mathbf{x} \quad &= \quad z[1 \quad 1 \quad 1]^{\mathrm{T}}
\end{aligned} \tag{A.12}
$$

Error dx, dy and dz correspond to the first, second and third component of $d\mathbf{x}$.

A.3 sp3 naming convention

The naming convention of sp3 files is the following:

- ESA0OPSFIN_YYYYDDDHH00_DUR_SMP_CNT.FMT

- ESA: 3-character center ID

- 0: Version ID

- OPS = Operation product

- FIN = Final, RAP = Rapid, ILT = Ultra-rapid

- YYYY: 4-character year

- DDD: 3-character day of year

- HH: 2-character hour of the day

- LEN: 3-character Product period

- SMP: 3-char sampling interval

- CNT: 3-character Content type

- FMT: 3-character Format of file

A.3.1 IONOS functional description

- **get_sp3.m** (sp3-d [*file*]) $\longrightarrow$ GNSS _ info [*struct*], PRN [*dict*], M [*array*]

    - I/ parses a sp3-d file from its filename.

    - O/ GNSS _ info contains epoch, number of epochs, number of satellites, time system and precision. PRN is the list of satellites. M has columns : {PRN letter (ASCII)}, {PRN number}, {X (ITRF, km)}, {Y (ITRF, km)}, {Z (ITRF, km)}, {Clock offset (μs)}

- **get_GNSS_vis.m** (PRN [*dict*], GNSS [*array*], CoG [*column*], SAT [*struct*], ANT [*struct*]) $\longrightarrow$ SKY [*struct*]

    - I/ PRN is dict of all satellites observed, GNSS is a matrix whose columns are, X [km], Y[km], Z[km] in ITRF frame, CoG is geodetic ITRF coordinates. Satellite and antenna configurations are parameters.

    - O/ SKY : structure with PRN, ITRS, NED, Azimuth, elevation, zenith and slant distance in antenna frame.

- **FilterConstellation.m** (x_GNSS [*array*], x_sc [*column*], SIMU [*struct*], SKY [*struct*], CONSTELLATION [*string*], mask [*double*]) $\longrightarrow$ SKY

  – I/ Origo position in ITRF coordinates, and GNSS satellites positions in ITRF and Azimuth / Elevation.

  – O/ Filter the satellites blocked by the Earth and below elevation mask.

- *SplitConstellation* : Position and visibility are grouped by constellations in structure fields. Requires (GNSS _ info) and position and visibility for all satellites at a given epoch.

- *av_all_gnss* : Computes the percentage of time with more than n satellites. Constellations can be selected one by ine or combined (e.g. 99% of time with more than 12 satellites, Galileo or GPS)

- *DOPS*: Computes GDOP, PDOP, TDOP, HDOP, VDOP from n satellites visible. Inputs are slant distance, spacecraft CoM in ITRF and transformation from .

- *process_GNSS* : initialisation of matrices with results (rows for epochs, columns for satellites). Computes $q_{\text{ITRF}\longrightarrow\text{NED}}$. If the quaternion $q_{\text{GCRF}\longrightarrow\text{SAT}}$ is not given, the quaternion is computed with $q_{\text{GCRF}\longrightarrow\text{ITRF}}$, $q_{\text{ITRF}\longrightarrow\text{NED}}$, $q_{\text{NED}\longrightarrow\text{SAT}}$. The set of 3-2-1 Euler angles (h, b, φ) from NED to SAT is computed. Unit vectors of NED, SAT, and ANT are computed and scaled for display. Visibility, DOPs, angular velocities are computed.

A.3.2 IERS convention analysis : library description

The following paragraph summarises the inputs and outputs of each library.

- lib_IERS: This library was implemented to automatise the extraction and analysis of Earth Orientation parameters. Three scripts were developed. For each script, functions are listed, with inputs, types and a description :

  – iers_access.py:

    * **getEOPs**
      (df [*Dataframe*], TAI [*double*], n_day [*double*], name [*string*])$\longrightarrow$ EOP [*double*]

      · Yields EOP at any epoch. df contains EOPs. TAI is MJD.

    * **getIndexFromTAIMJD** (TAI [*double*], df [*Dataframe*]) $\longrightarrow$ i [*double*].

      · i = row number of IERS table

    * **getTAIMJDFromIndex** (i [*double*], df [*Dataframe*]) $\longrightarrow$ TAI [*double*]

· TAI MJD of row n°i. Epoch described by output TAI is 0h00 UTC.

* **findValue** (TAI [*double*], df [*Dataframe*], name [*string*]) ⟶ EOP

· Yields latest EOP entry. Epoch of EOP is 0h00 UTC.

– iers_process.py:

* **iers_parsing** (filepath [*string*], iers_data [*Dataframe*]) ⟶ df_EOP [*Dataframe*].

· Indexing with number of days since 1972-01-01. Adds the following columns to the table provided by IERS : {Leap second},{Last leap second date},{TAI_MJD},{UT1_datetime},{TAI-UT1}.

• lib_time:

– time_conversion.py. The most important functions are listed below.

* UTC_date_2_TAI_MJD(UTC,df_in)

* TAI_MJD_2_TAI_date_u(TAI_MJD)

* TAI_MJD_2_TAI_date(V_TAI_MJD):

* UTC2TT(UTC, df_in)

* UTC2TAI(UTC, df_in)

* TAI2TT(TAI)

* TT2TAI(TT)

• lib_unit: Conversion between radians, degrees, and arcseconds.

• lib_frame: This library provides a simple way to convert a dataframe of ITRS coordinates to a dataframe of GCRS coordinates. Unit functions were developed to compute rotation matrices, and quaternion algebra.

– frame_conversion.py

* **EPHI** (M [*array*]) ⟶ **e** [*column*], Φ [*double*]

· Yields principal rotation axis and principal rotation angle.

* **Markley** (M [*array*]) ⟶ Quaternion q

· Quaternion is computed from DCM using Markley's method [63].

* **PositionITRS2GCRSMat** (r [*double*], Q [*array*], R [*array*], W [*array*]) ⟶

```python
def date2string(T_in):
    """Input : date, format = timestamp or string
       Output: strings"""

    T = str(T_in)

    datetime,date,time,hh,mm,ss,decimal = 7*[''] # init

    if '.' in T:
        datetime = T.split('.')[0]
        decimal = T.split('.')[1]
        if 'T' in datetime:
            date = datetime.split('T')[0]
            time = datetime.split('T')[1]
            hh,mm,ss = time.split(':')
        else:
            date = datetime.split()[0]
            time = datetime.split()[1]
            hh,mm,ss = time.split(':')

    elif 'T' in T:
        datetime = T
        date = T.split('T')[0]
        time = T.split('T')[1]
        hh,mm,ss = time.split(':')
    else:
        datetime = T
        date = T.split()[0]
        if len(T.split())==2:
            time = T.split()[1]
            hh,mm,ss = time.split(':')


    return T,datetime,date,time,hh,mm,ss,decimal
```

Figure A.3.1: Internal representation of time

· Converts a position expressed in ITRS to GCRS using the matrix transformation. The inverse transformation was also implemented.

* **PositionITRS2GCRSQuat** (r [*column*], Q [*array*], R [*array*], W [*array*]) $\longrightarrow$

· Converts a position expressed in ITRS to GCRS using the quaternion transformation. The inverse transformation was also implemented.

* **VelocityITRS2GCRSMat**(v_ITRF [*column*], omega [*double*], r [*column*], Q [*array*], R [*array*], W [*array*]) $\longrightarrow$ v_GCRF [*column*]

· Converts a velocity expressed in ITRS to GCRS using the matrix transformation. The inverse transformation was also implemented.

∗ **frame_validation**(M,M_ref,z) $\longrightarrow$ Φ [*double*], dx [*double*],dy [*double*],dz [*double*],3D [*double*]

· Yields rotational error Φ. Yields the associated range error along x,y,z axes and 3D error at altitude z.

TRITA-ABE-MBT-23509